Fritz-Haber-Institut der Max Planck Gesellschaft
Technische Universtät Berlin

Institut für Theoretische Physik

Fakultät II

Bachelor Thesis

Thermal Conductivities of Group IV and Group III-V Compound Semiconductors from First Principles

Paul Manuel Müller

Matriculation Number: 367494

January 31$^{\text{st}}$, 2018

Supervisors:

Prof. Dr. Andreas Knorr
Prof. Dr. Matthias Scheffler

Erklärung zur eigenständigen Anfertigung

Hiermit erkläre ich, dass die vorliegende Arbeit selbständig und eigenhändig sowie ohne unerlaubte fremde Hilfe und ausschließlich unter Verwendung der aufgeführten Quellen und Hilfsmittel angefertigt habe.

Berlin, January 31$^{\text{st}}$, 2018
Ort, Datum

Unterschrift

Abstract

Over the last decades, a first-principles assessment of anharmonic effects in solids has become possible. To date, non-perturbative molecular-dynamics based methodologies exists to account for all orders of anharmonicity and thus to treat these effects accurately. Nonetheless, perturbative approaches that only incorporate anharmonic effects to the lowest order are widely popular due their manageable computational cost. It is, however, yet unclear how severely the involved approximations affect the computed material properties. To shed light on this issue, thermal expansion coefficients and thermal conductivities of 35 group IV and group III-V compound semiconductors in the temperature range of $0\,\mathrm{K}$ to $1000\,\mathrm{K}$ using a perturbative approach, i.e., density-functional theory and phonon calculations based on the quasi harmonic approximation and the relaxation time approximation, respectively, are calculated. Particular focus was laid on the computational numerical parameters, so to reveal the intrinsic uncertainty associated to such perturbative calculations and their physical and numeric origin. The resulting thermal expansion coefficients reproduce the qualitative experimental trends, e.g., the negative thermal expansion of silicon below $100\,\mathrm{K}$. Similarly, the computed thermal conductivities reproduce qualitative experimental trends correctly, yielding for instance small thermal conductivities for heavy compounds and large ones for light systems. In all cases, accounting for mass defect scattering and lattice expansion improved the results considerably, yielding closer agreement with experiment. This comparison suggests that "good" thermal conductors are indeed reliably described by perturbative approaches, whereas "bad" thermal conductors are not: We find that the computed thermal conductivities deviate from the measured ones by up to $45.3\,\mathrm{WK^{-1}m^{-1}}$ ($77\,\%$) for compounds with thermal conductivities below 100 W/mK at 300 K. Since these deviations are not explainable within the intrinsic numeric uncertainty of the calculations, the computed results can serve as a reliable reference set, against which higher-order methods can be benchmarked.

Übersicht

In den letzten Jahrzehnten wurde eine grundlegende Bewertung von anharmonischen Effekten in Festköprern möglich. Heutzutage existieren nicht perturbative auf Molekulardynamik basierende Methoden um alle Ordnung der Anharmonizität zu berücksichtigen und so diese Effekte akkurat zu behandeln. Nichts desto trotz werden perturbative Ansätze, die anharmonische Effekte nur bis zur niedrigsten Ordnung berücksichtigen, oft verwendet, da ihre computionellen Kosten handhabbar sind. Es ist allerdings immer noch unklar wie stark die verwendeten Näherungen die berechneten Materialeigenschaften beeinflussen. Um Licht auf dieses Problem zu werfen, wurden thermische Ausdehnungskoeffizienten und thermische Leitfähigkeiten für 35 Gruppe IV und Gruppe III-V Halbleiter im Temperaturbereich zwischen $0\,K$ und $1000\,K$ mit einem perturbativen Ansatz berechnet. Der verwendete Ansatz nutzt Dichtefunktionaltheorie und Phononenrechnungen basierend jeweils auf der quasiharmonischen Näherung und der Relaxationszeitnäherung. Besonderer Focus wurde auf die numerischen Parameter gelegt, um die intrinsische Ungenauigkeit von Rechnungen auf Basis dieser perturbativen Ansätze und deren Herkunft aufzuklären. Die berechneten thermische Ausdehnungskoeffizienten reproduzieren die qualitativen experimentellen Trends, wie zum Beispiel die negative thermische Ausdehnung von Silizium unter $100\,K$. Ähnlich korrekt reproduzieren die berechneten thermischen Leitfähigkeiten die qualitativen experimentellen Trends, zum Beispiel geringe thermische Leitfähigkeiten von schweren Materialien und hohe thermische Leitfähigkeiten von leichten Materialien. In allen Fällen verbesserte die Betrachtung von Massdefektstreuung und thermischer Ausdehnung die Übereinstimmung mit dem Experiment beträchtlich. Dieser Vergleich legt nahe, dass „gute "thermische Leiter tatsächlich durch perturbative Ansätze beschrieben werden können und schlechte nicht: Die berechneten thermischen Leitfähigkeiten für Materialien mit thermischen Leitfähigkeiten unter $100\,WK^{-1}m^{-1}$ weichen bis zu $45.3\,WK^{-1}m^{-1}$ ($77\,\%$) von den gemessenen ab. Da diese Differenzen nicht durch intrinisische numerische Unsicherheiten erklären lassen, können die berechneten Ergebnisse als Refernzset dienen, an der sich Methoden höherer Ordnung messen lassen.

Acknowledgments

First, I want to thank my friends and my family for supporting me all my life and especially while writing this thesis. I want to thank Sebastian Garcia particularly for proofreading my thesis.

Furthermore, I want to thank Prof. Dr. Andreas Knorr and Prof. Dr. Matthias Scheffler for making this thesis possible in the first place.

My special thanks go to Dr. Christian Carbongo and Florian Knoop who supervised my work, had always meaningful suggestions to improve this thesis and were able to answer all my questions.

Contents

1. Introduction

Both efficient heat transport and insulation are of great interest in technical applications and scientific studies likewise. For example, turbines and combustion engines can be insulated by thermal barrier coatings to improve their durability and efficiency. The efficiency is increased due to higher possible operational temperatures [1]. Other applications can be found in the development of thermoelectric materials which allow for direct conversion of heat into electrical power or vice versa [2]. Since the thermoelectric figure of merit depends on the thermal conductivity, controlling it is important to increase efficiency. Moreover, the application of high thermal conductance materials is crucial in electronics, as in electronic components local "hot spots" of high heat can originate. Enhancing thermal conductivity to remove heat from these spots can significantly improve lifetimes of these devices and increase the temperature operation range. These components mostly contain semiconductors; thus, their thermal conductivity is of great interest. Frequently used semiconductors are for example silicon, gallium nitride or gallium arsenide. They all are part of the group IV and group III-V compound semiconductors. This work will investigate the thermal properties of the materials of these groups in their cubic (zincblende or diamond) structure and their hexagonal wurtzite structure by calculations from first principles. Various approaches to describe and compute phonon thermal conductivities from first-principles exist, which can generally be classified by the extent of which anharmonic effects are accounted for: a) *Perturbative* approaches account for the lowest order of anharmonicity via third-order (and possibly fourth-order) force constants computed in the 0 K limit [3]. The thermal conductivities are then computed by solving the linearized Boltzmann transport equation either exactly [4] or in the relaxation time approximation [3]. b) *Temperature-dependent* approaches improve the description of anharmonic effects by determining the third-order (and possibly fourth-order) force constants at finite-temperatures, e.g., via molecular dynamics [5]. c) *Non-perturbative* approaches rely on molecular-dynamics simulations and thus account for all orders of anharmonicity. In this case, the thermal conductivity is computed using Green-Kubo linear response theory [6]. In spite of the fact that such more accurate approaches exist, the *perturbative* approach (a) based on third-order force constants is still the most widespread due to its manageable computational cost. The accuracy of such calculations is, however still topic of scientific debate: Depending on the numerical parameters used in this approach, literature reports quite different thermal conductivity values between 130 and $160 \, \mathrm{WK^{-1}m^{-1}}$ even for silicon at 300 K [7], a material and temperature range for which higher-order anharmonicities are expected to be negligible. Understanding the numerical uncertainty of such calculations is thus one of the main focuses of this work. Therefore, convergence tests were run for all the different numerical parameters, thus yielding a systematic and reliable set of benchmark calculations. This allows to study trends of the thermal conductivity across chemical and structural space. The comparison with experimental values in Sec. 4.4 then enables to identify the materials for which such a perturbative approach appears to work and the materials for which it appears to fail, thus providing a reliable benchmark set for testing higher-order methodologies such as (b) and (c).

This work is structured as follows:

In Sec. 2, the underlying theory is discussed. The many-body problem and its reformulation through density functional theory is discussed. The harmonic approximation and the derivation of the thermal properties through the dynamical matrix are performed. The picture is extended to the perturbative treatment of anharmonic effects with the thermal conductivity in the relaxation time approach and the thermal expansion in the quasi harmonic approximation.

In Sec. 3, the computational parameters for force calculations through the all-electron, full-potential electronic structure code *FHI-aims* [8], the second-order force constants and harmonic properties with *phonopy* [9] and the thermal conductivity with *phono3py* [10] are tested for the example of silicon.

In Sec. 4, harmonic properties, thermal expansion and thermal conductivity are discussed for silicon. Moreover, the thermal expansion coefficients for 35 group IV and group III-V compound semiconductors in zincblende/diamond and wurtzite structure are calculated within the quasi harmonic approximation. Thermal conductivities are calculated for the same class of materials. The discussed approximations are applied and mass defects due to isotopes are neglected. Then, these mass defects are included in the calculations. Lastly, the influence of thermal expansion of the lattice on the thermal conductivity is examined. Therefore, the thermal expansion calculations of this work are applied to simulate expanded lattice sizes.

In Sec. 5, the results of this work are summarized and a critical view of this work is given.

2. Theoretical Background

2.1. Many-Body Problem

Under the neglection of relativistic effects, a system of N_{el} electrons with positions $\boldsymbol{r} = (\boldsymbol{r}_1, ..., \boldsymbol{r}_{N_{\mathrm{el}}})$ and charge $-e$ and N_{nuc} nuclei with positions $\boldsymbol{R} = (\boldsymbol{R}_1, ..., \boldsymbol{R}_{N_{\mathrm{nuc}}})$ and charge $Z_I \cdot e$ can be generally described by the time independent Schrödinger equation

$$H(\boldsymbol{r}, \boldsymbol{R})\Psi(\boldsymbol{r}, \boldsymbol{R}) = E\Psi(\boldsymbol{r}, \boldsymbol{R}) , \tag{2.1.1}$$

where $H(\boldsymbol{r}, \boldsymbol{R})$ is the Hamiltonian which describes the system, E is its energy and $\Psi(\boldsymbol{r}, \boldsymbol{R})$ is the many-body wave function. The Hamiltonian can be split into [11]

$$H = T_{\mathrm{nuc}} + T_{\mathrm{el}} + V_{\mathrm{nuc\text{-}nuc}} + V_{\mathrm{el\text{-}el}} + V_{\mathrm{el\text{-}nuc}} , \tag{2.1.2}$$

where T_{nuc} and T_{el} are the kinetic energies of the nuclei and electrons with the masses M_I and m_{el} respectively,

$$T_{\mathrm{nuc}} = \sum_{I=1}^{N_{\mathrm{nuc}}} \frac{\boldsymbol{P}_I{}^2}{2M_I} , \qquad T_{\mathrm{el}} = \sum_{i=1}^{N_{\mathrm{el}}} \frac{\boldsymbol{p}_i{}^2}{2m_{\mathrm{el}}} . \tag{2.1.3}$$

Moreover, $V_{\mathrm{nuc\text{-}nuc}}$, $V_{\mathrm{el\text{-}el}}$, and $V_{\mathrm{el\text{-}nuc}}$ describe the electrostatic interactions between nuclei-nuclei, electrons-electrons, and electrons-nuclei:

$$V_{\mathrm{nuc\text{-}nuc}} = \frac{1}{2}\frac{e^2}{4\pi\epsilon_0} \sum_{\substack{I,J=1 \\ I \neq J}}^{N_{\mathrm{nuc}},N_{\mathrm{nuc}}} \frac{Z_I Z_J}{|\boldsymbol{R}_I - \boldsymbol{R}_J|} , \tag{2.1.4}$$

$$V_{\mathrm{el\text{-}el}} = \frac{1}{2}\frac{e^2}{4\pi\epsilon_0} \sum_{\substack{i,j=1 \\ i \neq j}}^{N_{\mathrm{el}},N_{\mathrm{el}}} \frac{1}{|\boldsymbol{r}_i - \boldsymbol{r}_j|} , \tag{2.1.5}$$

$$V_{\mathrm{el\text{-}nuc}} = -\frac{e^2}{4\pi\epsilon_0} \sum_{I=1}^{N_{\mathrm{nuc}}} \sum_{i=1}^{N_{\mathrm{el}}} \frac{1}{|\boldsymbol{R}_I - \boldsymbol{r}_i|} Z_I . \tag{2.1.6}$$

Finding a general solution $\Psi(\boldsymbol{r}, \boldsymbol{R})$ which solves Eq. (2.1.1) is a non-trivial problem. Due to the mass difference $m_{\mathrm{el}} \ll M_I$, one possible simplification consists in decoupling the motion of the light electrons from the heavy nuclei, under the assumption that the electrons adjust instantaneously to changes in the position of the nuclei. This approximation is called the Adiabatic or Born-Oppenheimer approximation: Although this approximation is certainly not valid under all possible circumstances, its validity is assumed in the rest of this work. Mathematically, it can be expressed by a product ansatz for the wave function $\Psi(\boldsymbol{r}, \boldsymbol{R}) = \Psi_{\mathrm{el}}(\boldsymbol{r}, \{\boldsymbol{R}\})\Psi_{\mathrm{nuc}}(\boldsymbol{R})$. Hereby $\{\boldsymbol{R}\}$ means that the nuclei positions enter the electronic wave

function $\Psi_{\text{el}}(\boldsymbol{r}, \{\boldsymbol{R}\})$ as parameters. The wave function of the nuclei $\Psi_{\text{nuc}}(\boldsymbol{R})$ depends on the positions of the nuclei $\boldsymbol{R}$ but is independent of the positions of the electrons $\boldsymbol{r}$. Within this approximation the Schrödinger equation separates to

$$\underbrace{(T_{\text{el}} + V_{\text{el-nuc}}(\boldsymbol{r}, \{\boldsymbol{R}\}) + V_{\text{el-el}}(\boldsymbol{r}))}_{H_{\text{el}}} \Psi_{\text{el}}(\boldsymbol{r}, \{\boldsymbol{R}\}) = E_{\text{el}}(\{\boldsymbol{R}\})\Psi_{\text{el}}(\boldsymbol{r}, \{\boldsymbol{R}\}) , \qquad (2.1.7)$$

$$\underbrace{(T_{\text{nuc}} + V_{\text{nuc-nuc}}(\boldsymbol{R}) + E_{\text{el}}(\{\boldsymbol{R}\}))}_{H_{\text{nuc}}} \Psi_{\text{nuc}}(\boldsymbol{R}) = E_{\text{nuc}}\Psi_{\text{nuc}}(\boldsymbol{R}) . \qquad (2.1.8)$$

Equation (2.1.7) gives the electronic Schrödinger equation with the electronic energy $E_{\text{el}}(\{\boldsymbol{R}\})$. The electronic energy enters Eq. (2.1.8) as an additional potential for the nuclei. Together with the nuclei-nuclei repulsion, it forms the potential-energy surface, on which the atoms move.

2.1.1. Density-Functional Theory

Even with the simplification as made in the Born-Oppenheimer approximation above, the problem of finding the ground state energy is still complicated. One approach to solve this problem is through *density-functional theory* (DFT) for which Walter Kohn was awarded the Nobel prize in chemistry in 1998. In DFT, the ground state is expressed in terms of the electron density n, which only depends on three cartesian coordinates, as opposed to the original $3\,N_{\text{el}}$ coordinates.

The idea behind DFT can be expressed in two statements as derived by Hohenberg and Kohn [12]:

- For an interacting electron system, there is a bijection between the ground state density and the external potential.

- If an energy functional $E_V[n]$ exists, the density which minimizes this functional is the ground state density.

The energy functional can be written as [12]

$$E_V[n] = F_{\text{HK}}[n] + \int \mathrm{d}^3 r\, V(\boldsymbol{r})n(\boldsymbol{r}) , \qquad (2.1.9)$$

$$\text{with} \quad F_{\text{HK}}[n] = \langle \Psi[n]|T + W|\Psi[n]\rangle , \qquad (2.1.10)$$

where F_{HK} includes all electron-electron interactions W as well as the kinetic energy. The potential V represents all interactions of the electrons with an external potential. In the case discussed here, it represents the interaction of the electrons with the nuclei. This can be written as

$$\int \mathrm{d}^3 r\, V(\boldsymbol{r})n(\boldsymbol{r}) = -\sum_I \int \frac{Z_I n(\boldsymbol{r})}{|\boldsymbol{r} - \boldsymbol{R}_I|} \mathrm{d}^3 r . \qquad (2.1.11)$$

Accordingly, DFT is "only" an elegant reformulation of the Schrödinger equation. In this form, it has only little practical use, since, so far, there has not been found any analytical expression for the functional F_{HK}. For practical applications, the Kohn-Sham formalism

can be applied to recast the equations into a form that allows to find useful approximation schemes.

Kohn-Sham Formalism

The essence of the Kohn-Sham formalism is that the electron density is expressed by N_{el} non-interacting single-particle wave functions $\varphi_i(\boldsymbol{r})$ as

$$n(\boldsymbol{r}) = \sum_{i}^{N_{el}} |\varphi_i(\boldsymbol{r})|. \tag{2.1.12}$$

By this means, Eq. (2.1.9) can be rewritten so that the single-particle wave functions have to obey a different, formally non-interacting single-particle Schrödinger equation, i.e, the Kohn-Sham equation [13]

$$\left(-\frac{\hbar^2}{2m}\nabla^2 + V_{eff}(\boldsymbol{r}) \right) \varphi_i(\boldsymbol{r}) = \epsilon_i \varphi_i(\boldsymbol{r}) , \tag{2.1.13}$$

$$\text{with} \quad V_{eff}(\boldsymbol{r}) = V_0(\boldsymbol{r}) + \int \mathrm{d}^3 r' \frac{n(\boldsymbol{r})}{|\boldsymbol{r}-\boldsymbol{r}'|} + V_{xc}\left([n(\boldsymbol{r})], \boldsymbol{r}\right) , \tag{2.1.14}$$

with the effective potential V_{eff}, where $V_0(\boldsymbol{r})$ is the external potential which includes the electrostatic potential of the nuclei. The second term in $V_{eff}(\boldsymbol{r})$ gives the Hartree contribution of the electron-electron interaction. The so called exchange correlation potential $V_{xc}([n(\boldsymbol{r})], \boldsymbol{r})$ incorporates all many-body effects. As the potential $V_{eff}(\boldsymbol{r})$ includes the ground state density itself the Kohn-Sham equation has to be solved self-consistently. The ground state energy E_0 becomes

$$E_0 = \sum_{i=1}^{occupied} \epsilon_i - \frac{1}{2} \int\int \mathrm{d}^3 r \mathrm{d}^3 r' n(\boldsymbol{r}) W(\boldsymbol{r}, \boldsymbol{r}') n(\boldsymbol{r}') + \tag{2.1.15}$$

$$E_{xc}[n] - \int \mathrm{d}^3 r V_{xc}\left([n(\boldsymbol{r})], \boldsymbol{r}\right) n(\boldsymbol{r}) \quad , \text{with}$$

$$E_{xc} = F_{HK}[n] - \frac{1}{2} \int\int \mathrm{d}^3 r \mathrm{d}^3 r' n(\boldsymbol{r}) W(\boldsymbol{r}, \boldsymbol{r}') n(\boldsymbol{r}') - T_S[n] , \tag{2.1.16}$$

with the kinetic energy of the non-interacting system $T_S[n]$ and the electron-electron interactions expressed through the term with $W(\boldsymbol{r}, \boldsymbol{r}')$. A detailed introduction of the Kohn-Sham formalism can be found for example in Ref. [14]. In addition, if the potential $V_{eff}(\boldsymbol{r}) = V_{eff}(\boldsymbol{r} + \boldsymbol{R})$ is periodic due to the crystal symmetry, one can choose a Bloch ansatz for the wave function in the volume of the primitive unit cell V_0 [11]

$$\varphi_{i,\boldsymbol{k}}(\boldsymbol{r}) = \frac{1}{\sqrt{V_0}} e^{i\boldsymbol{k}\boldsymbol{r}} u_{i,\boldsymbol{k}}(\boldsymbol{r}) , \tag{2.1.17}$$

$$u_{i,\boldsymbol{k}}(\boldsymbol{r}) = u_{i,\boldsymbol{k}}(\boldsymbol{r} + \boldsymbol{R}) , \tag{2.1.18}$$

with a periodic function $u_{i,\boldsymbol{k}}(\boldsymbol{r})$ and the crystal momentum $\boldsymbol{k}$ as additional quantum number. The $\boldsymbol{k}$'s are restricted to the first Brillouin zone in the reciprocal space, which corresponds to the primitive unit cell in real space. The resulting differential equation leads to unique

solutions. Inserting the ansatz in Eq. (2.1.13) yields a differential equation for the $u_{i,\boldsymbol{k}}(\boldsymbol{r})$,

$$\left[\frac{\hbar^2}{2m} \left(-\mathrm{i}\boldsymbol{\nabla} + \boldsymbol{k} \right)^2 + V_{\mathrm{eff}}(\boldsymbol{r}) \right] u_{i,\boldsymbol{k}}(\boldsymbol{r}) = \epsilon(\boldsymbol{k}) u_{i,\boldsymbol{k}}(\boldsymbol{r}) \ . \tag{2.1.19}$$

Formally, this equation must be solved for every $\boldsymbol{k}$ in the first Brillouin zone. In practice, a finite grid of sampling points in the first Brillouin zone is typically sufficient to achieve accurate and converged calculations.

Approximation of the Exchange-Correlation Functional

Even though the Kohn-Sham formalism as discussed above is formally exact there is no analytical representation for the exchange-correlation functional known. However, there are multiple approximation schemes of which two will be explained briefly in the following.

Local-Density Approximation (LDA): In the LDA the exchange-correlation energy E_{xc} gets approximated at every point $\boldsymbol{r}$ with the value of the corresponding exchange-correlation energy of a homogeneous electron gas $\epsilon_{\mathrm{xc}}^{\mathrm{hom}}$ [14],

$$E_{\mathrm{xc}}^{\mathrm{LDA}} = \int \mathrm{d}^3 r \, \epsilon_{\mathrm{xc}}^{\mathrm{hom}}[n(\boldsymbol{r})] n(\boldsymbol{r}) \ . \tag{2.1.20}$$

General Gradient Approximation (GGA): To improve the LDA, the GGA can be made in the spirit of a Taylor expansion. Therefore, the local exchange-correlation energy becomes dependent not only on the local electron density, but also its local derivative $\boldsymbol{\nabla}_{\boldsymbol{r}} n(\boldsymbol{r})$

$$E_{\mathrm{xc}}^{\mathrm{GGA}} = E_{\mathrm{xc}}^{\mathrm{GGA}}[n(\boldsymbol{r}), \nabla_{\boldsymbol{r}} n(\boldsymbol{r})] \ . \tag{2.1.21}$$

There are many different flavours of this approximation due to some freedom in the parametrization of $E_{\mathrm{xc}}^{\mathrm{GGA}}$. Perdew–Burke-Ernzerhof (PBE) [15] and its adaption for solids PBEsol [16] are two commonly used in solid state physics and will be used in this work as well.

Hellmann-Feynman Theorem

In the case of the general quantum-mechanical problem, the Hellmann-Feynman theorem can be used in Kohn-Sham-DFT to calculate the first derivatives of the energy, namely the forces on the atoms [17]. The theorem states that for a time independent Hamiltonian H with eigenfunctions Ψ_λ the derivative of the total energy E_λ with respect to a parameter λ (in this work, the displacement) is

$$F_\lambda = \frac{\mathrm{d}E_\lambda}{\mathrm{d}\lambda} = \left\langle \Psi_\lambda \left| \frac{\mathrm{d}H}{\mathrm{d}\lambda} \right| \Psi_\lambda \right\rangle \ , \tag{2.1.22}$$

so that for $\lambda = \boldsymbol{R}_I$ and the above discussed crystal Hamiltonian (see Eq. (2.1.13))

$$F_I = \sum_{J, J \neq I} \frac{Z_I Z_J}{|\boldsymbol{R}_I - \boldsymbol{R}_J|^3} (\boldsymbol{R}_I - \boldsymbol{R}_J) - \int \mathrm{d}^3 r \, n(\boldsymbol{r}) \sum_I \frac{Z_I}{|\boldsymbol{r} - \boldsymbol{R}_I|^3} (\boldsymbol{r} - \boldsymbol{R}_I) \ , \tag{2.1.23}$$

with the last equation being the force on the nuclei in the electrostatic field of the electron density and the other nuclei [8]. As the wave function Ψ_λ can be mapped on the electron density, the forces become a functional of the electron density. The used DFT code *FHI-aims* includes some more contributions to the forces [8]. Firstly, electrostatic multipole derivatives which arise due to a truncation of the electrostatic potential. Secondly, the Pulay forces which arise due to basis function sets which are not independent of the atomic positions, and thirdly relativistic corrections.

2.2. Harmonic Approximation

The position of the kth atom in the Ith unit cell in the crystal is described as a displacement $\boldsymbol{u}_{Ik}$ around the equilibrium position $\boldsymbol{R}^0_{Ik}$. The equilibrium position can be split into the position of the unit cell $\boldsymbol{R}_I$ and the position of the atom in the unit cell $\boldsymbol{r}_k$,

$$\boldsymbol{R}_{Ik} = \boldsymbol{R}^0_{Ik} + \boldsymbol{u}_{Ik} = \boldsymbol{R}_I + \boldsymbol{r}_k + \boldsymbol{u}_{Ik} \ . \tag{2.2.1}$$

Due to the translational symmetry of the lattice, the vector $\boldsymbol{R}_I - \boldsymbol{R}_J$ describes a lattice vector again. The dynamics of the system is determined by the Hamilton operator (see Eq. (2.1.8))

$$H = \sum_{I,k} \frac{\boldsymbol{P}^2_{Ik}}{2M_{Ik}} + \Phi(\boldsymbol{R}) \ . \tag{2.2.2}$$

The potential energy operator $\Phi(\boldsymbol{R} = (\boldsymbol{R}_{1,1}, ..., \boldsymbol{R}_{N,n}))$ is determined by the positions of the atoms, where N is the number of unit cells and n the number of atoms in the unit cells. The potential energy can be expanded into a Taylor series around the equilibrium positions, where α denotes a cartesian component in the three dimensional space,

$$\begin{aligned}
\Phi = \Phi_0 &+ \sum_{I,k} \sum_\alpha \left. \frac{\partial \Phi}{\partial R_{Ik\alpha}} \right|_{R^0_{Ik\alpha}} \cdot u_{Ik\alpha} \\
&+ \frac{1}{2} \sum_{I,k,J,l} \sum_{\alpha,\beta} \left. \frac{\partial^2 \Phi}{\partial R_{Ik\alpha} \partial R_{Jl\beta}} \right|_{R^0_{Ik\alpha}, R^0_{Jl\beta}} \cdot u_{Ik\alpha} u_{Jl\beta} + \mathcal{O}(u^3) \ .
\end{aligned} \tag{2.2.3}$$

In the equilibrium position, where the energy is minimal, the first order term vanishes. The zeroth order term is a constant and can be chosen to be zero. In the harmonic approximation terms higher than 3rd order are neglected. The resulting potential is completely determined by the second order derivative,

$$\Phi_{Ik\alpha, Jl\beta} = \left. \frac{\partial^2 \Phi}{\partial R_{Ik\alpha} \partial R_{Jl\beta}} \right|_{R^0_{Ik\alpha}, R^0_{Jl\beta}} = \left. \frac{\partial F_{Ik\alpha}}{\partial R_{Jl\beta}} \right|_{R^0_{Jl\beta}} \sim \lim_{d \to 0} \frac{F_{Ik\alpha}(\boldsymbol{R}^0_{Ik} + d \cdot \boldsymbol{e}_{Jl\beta})}{d} \ , \tag{2.2.4}$$

i.e., the Hessian of the system, commonly identified as *harmonic force constants* because the first derivative of the potential gives the force $F_{Ik\alpha}$. Note that the last expression introduces the finite difference method, which allows to compute the required derivatives in an approximative fashion: The derivative of the force gets approximated by the difference of the force of two atoms with a finite displacement distance of d and the direction vector $\boldsymbol{e}_{Jl\beta}$.

If one atom is to be chosen in the equilibrium position its force is zero and only the force of one displaced atom has to be calculated. This is the simplest approach for determining force constants, the analytical computation of which requires the application of perturbation theory.

The Hamiltonian can be brought into the standard form after rescaling positions $\boldsymbol{u}$ and momenta $\boldsymbol{p}$ and introducing the dynamical matrix,

$$(D)_{Ik\alpha,Jl\beta} = \frac{1}{\sqrt{M_{Ik}M_{Jl}}}\Phi_{Ik\alpha,Jl\beta} \; , \tag{2.2.5}$$

$$H = \frac{1}{2}\left(\boldsymbol{p}^T\boldsymbol{p} + \boldsymbol{u}^T\underline{\underline{D}}\boldsymbol{u}\right) \; . \tag{2.2.6}$$

Since $\underline{\underline{\Phi}}$ is a real, symmetric, and positive definite matrix, the dynamical matrix shares these properties, so it can be diagonalized.

Equations of Motion

The classical equations of motion derived from the harmonic potential can be written as

$$M_k\ddot{u}_{Ik\alpha} = -\frac{\partial\Phi}{\partial u_{Ik\alpha}} = -\sum_{Jl\beta}\Phi_{Ik\alpha,Jl\beta} \cdot u_{Jl\beta} \; , \tag{2.2.7}$$

with $\Phi_{Ik\alpha,Jl\beta}$ given by Eq. (2.2.4). By dropping the unit cell index I in the mass M_{Ik}, a perfect crystal without disorder is considered. Moreover, the matrix $\underline{\underline{\Phi}}$ does not depend on the lattice vectors $\boldsymbol{R}_I$ and $\boldsymbol{R}_J$ separately but only on their difference due to the translational symmetry of the crystal,

$$\Phi_{Ik\alpha,Jl\beta} = \Phi_{k\alpha,l\beta}\left(\boldsymbol{R}_I - \boldsymbol{R}_J\right) \; . \tag{2.2.8}$$

The same holds for the dynamical matrix. The time dependent, Bloch like ansatz with time independent coefficients $w_{k\alpha}$ and the reciprocal space vector $\boldsymbol{q}$

$$u_{Ik\alpha} = \frac{w_{k\alpha}e^{i\boldsymbol{q}\boldsymbol{R}_I}}{\sqrt{M_k}}e^{-i\omega t} \; , \tag{2.2.9}$$

solves Eq. (2.2.7). Calculating the equation of motion with this ansatz yields an eigenvalue equation for the time independent $w_{k\alpha}$,

$$\omega^2 w_{k\alpha} = \sum_{l\beta}\sum_{I}D_{k\alpha,l\beta}(\boldsymbol{R}_I - \boldsymbol{R}_J)e^{i\boldsymbol{q}(\boldsymbol{R}_I - \boldsymbol{R}_J)}w_{l\beta} \; , \tag{2.2.10}$$

with the dynamical matrix as defined in Eq. (2.2.5). Due to the translational symmetry of the systems, $\boldsymbol{R}_J$ can be chosen to be zero. Furthermore, the definition

$$D_{k\alpha,l\beta}(\boldsymbol{q}) = \sum_{I}D_{k\alpha,l\beta}(\boldsymbol{R}_I)e^{-i\boldsymbol{q}\boldsymbol{R}_I} \; , \tag{2.2.11}$$

allows to evaluate the eigenvalue equation,

$$\omega^2 w_{k\alpha} = \sum_{l\beta} D_{k\alpha,l\beta}(\boldsymbol{q}) w_{l\beta} \ . \tag{2.2.12}$$

This simplifies the equation of motion in Eq. (2.2.7) to an eigenvalue problem of the $3\,n \times 3\,n$ dynamical matrix. At each crystal momentum $\boldsymbol{q}$, this gives $3\,n$ eigenvalues $\omega_{\boldsymbol{q}s}$ with the band index $s \in [1, 3\,n]$ and $3\,n$ dimensional eigenvectors $\boldsymbol{e}_k^{(s)}$ respectively. With this, the solution of the equation of motion Eq. (2.2.7) becomes

$$\boldsymbol{u}_{Ik}^{(s)} = \frac{1}{\sqrt{M_k}} \boldsymbol{e}_k^{(s)} \mathrm{e}^{\mathrm{i}(\boldsymbol{q}\boldsymbol{R}_I - \omega_{\boldsymbol{q}s}t)} \ . \tag{2.2.13}$$

With the calculated phonon dispersion $\omega_{\boldsymbol{q}s}$, one can in principle obtain all properties of the system.

Supercell approach

The evaluation of the Fourier transformed dynamical matrix, Eq. (2.2.11), is still a sum over all unit cells. However, the forces of an atom on its surrounding decay with the distance so that one can truncate the sum and only include atoms in a finite size supercell. The forces decay with negative powers of $|\boldsymbol{R}_I - \boldsymbol{R}_J|$ depending on the type of the force. Consequently the force constants decay as well with higher distances between the atoms. Note that higher order force constants tend to decay faster.

Quantum Mechanical Harmonic Oscillator

With the symmetric, diagonalisable dynamical matrix, the quantum mechanical Hamiltonian in the harmonic approximation can brought into the from

$$H = \sum_{\boldsymbol{q}} \sum_s^{nd} \hbar\omega_{\boldsymbol{q}s} \left(n_{\boldsymbol{q}s} + \frac{1}{2} \right) \ , \tag{2.2.14}$$

with the mode dependent phonon occupation number $n_{\boldsymbol{q}s} = a_{\boldsymbol{q}s}^\dagger a_{\boldsymbol{q}s}$ and the creation and annihilation operators

$$a_{\boldsymbol{q}s}^\dagger = \sqrt{\frac{\omega_{\boldsymbol{q}s}}{2\hbar}} \left(u_{\boldsymbol{q}s} + \frac{ip_{\boldsymbol{q}s}}{\omega} \right) \ , \tag{2.2.15}$$

$$a_{\boldsymbol{q}s} = \sqrt{\frac{\omega_{\boldsymbol{q}s}}{2\hbar}} \left(u_{\boldsymbol{q}s} - \frac{ip_{\boldsymbol{q}s}}{\omega} \right) \ , \tag{2.2.16}$$

$$\left[a_{\boldsymbol{q}s}, a_{\boldsymbol{q}'s'}^\dagger \right] = \delta_{s,s'}\delta_{\boldsymbol{q},\boldsymbol{q}'} \ , \quad \left[u_{\boldsymbol{q}s}, p_{\boldsymbol{q}'s'} \right] = \mathrm{i}\hbar\delta_{s,s'}\delta_{\boldsymbol{q},\boldsymbol{q}'} \ . \tag{2.2.17}$$

The essence of the solutions is that one finds basic excitations of the energy $\hbar\omega_{\boldsymbol{q}s}$ which are called phonons in the case of lattice vibrations. For more details see for example Ref. [18].

Thermal Properties

With Eq. (2.2.14) the energy of the phonon system E becomes

$$\langle n_{\boldsymbol{q}s}^0 \rangle = \frac{1}{\exp\left(\frac{\hbar\omega_{\boldsymbol{q}s}}{k_{\mathrm{B}}T}\right) - 1} \; , \tag{2.2.18}$$

$$E = \sum_{\boldsymbol{q},s} \hbar\omega_{\boldsymbol{q}s} \left(\frac{1}{2} + \langle n_{\boldsymbol{q}s}^0 \rangle\right) \; . \tag{2.2.19}$$

Here, $\langle n_{\boldsymbol{q}s}^0 \rangle$ is the occupation number of the phonon mode, which is given through the Bose-Einstein distribution. The heat capacity at constant volume can be calculated directly from the temperature derivative of the energy:

$$c_V = \frac{1}{V}\left.\frac{\partial E}{\partial T}\right|_V = \frac{1}{V}\sum_{\boldsymbol{q},s} k_{\mathrm{B}} \left(\frac{\hbar\omega_{\boldsymbol{q}s}}{k_{\mathrm{B}}T}\right)^2 \frac{\exp\left(\frac{\hbar\omega_{\boldsymbol{q}s}}{k_{\mathrm{B}}T}\right)}{\left(\exp\left(\frac{\hbar\omega_{\boldsymbol{q}s}}{k_{\mathrm{B}}T}\right) - 1\right)^2} \; , \tag{2.2.20}$$

$$= \frac{1}{V}\sum_{\boldsymbol{q},s} c_{\boldsymbol{q}s} \; . \tag{2.2.21}$$

Here, $c_{\boldsymbol{q}s}$ defines the mode heat capacity. In the high temperature limit, the heat capacity approaches the classical Dulong-Petit result $c_V = 3Nk_{\mathrm{B}}/V$, where N is the total number of atoms. For low temperatures, the heat capacity is approximately proportional to T^3 as in the Debye model [19]. Moreover, the thermodynamic partition function can be calculated within the solution of the harmonic problem [19]

$$Z = \prod_{\boldsymbol{q},s} \frac{\exp\left(\frac{-\hbar\omega_{\boldsymbol{q}s}}{2k_{\mathrm{B}}T}\right)}{1 - \exp\left(\frac{-\hbar\omega_{\boldsymbol{q}s}}{k_{\mathrm{B}}T}\right)} \; . \tag{2.2.22}$$

With this, the Helmholtz free energy F becomes [19]

$$F = -k_{\mathrm{B}}T\ln(Z) = \frac{1}{2}\sum_{\boldsymbol{q},s} \hbar\omega_{\boldsymbol{q}s} + k_{\mathrm{B}}T\sum_{\boldsymbol{q},s} \ln\left(1 - \exp\left(\frac{-\hbar\omega_{\boldsymbol{q}s}}{k_{\mathrm{B}}T}\right)\right) \; . \tag{2.2.23}$$

Furthermore, the entropy can be directly calculated from the free energy [20],

$$S = -\left.\frac{\partial F}{\partial T}\right|_V = \sum_{\boldsymbol{q}s} \frac{\hbar\omega_{\boldsymbol{q}s}}{T}\frac{1}{\exp\left(\frac{\hbar\omega_{\boldsymbol{q}s}}{k_{\mathrm{B}}}\right) - 1} - k_{\mathrm{B}}\ln\left(1 - \exp\left(\frac{-\hbar\omega_{\boldsymbol{q}s}}{k_{\mathrm{b}}}\right)\right) \; . \tag{2.2.24}$$

Density of States

The density of states $g(\omega)$ (DOS), which is a useful tool for computation of above properties, gives the number of states in a given energy interval $\mathrm{d}\omega$, [21]

$$g(\omega)\mathrm{d}\omega = \frac{\Omega}{(2\pi)^3}\sum_{s}\int_{\omega=\mathrm{const.}} \frac{\mathrm{d}f_{\boldsymbol{q}}}{|\nabla_{\boldsymbol{q}}\omega_{\boldsymbol{q}s}|}\mathrm{d}\omega \; , \tag{2.2.25}$$

with the volume of the Brillouin zone Ω. This formula shows the correlation between density of states and the band structure ω_{qs}. Flat bands result in high DOS. For extrema in the band structure this can even lead to points where the DOS is not smooth anymore or can even diverge; these are called van Hove singularities. A short discussion of the phonon dispersion relation can be found in App. A.

2.3. Thermal Conductivity

In general, a temperature gradient leads to heat conduction through particle diffusion or convection and thermal radiation within the material. Thermal radiation is usually a major contribution at high temperatures and convection is only dominant in fluids and gases. In solid state, heat is conducted by free electrons and quasi-particles such as phonons [22]. Due to the minor presence of free electrons, phonons give the major contribution in (pristine or moderately doped) semiconductors [3], so that only phononic heat conduction has to be considered. The thermal conductivity $\underline{\underline{\kappa}}$ is a second order tensor and macroscopically defined through Fourier's law [11]

$$\boldsymbol{Q} = -\underline{\underline{\kappa}}\boldsymbol{\nabla}T \; . \tag{2.3.1}$$

Here, $\boldsymbol{Q}$ is the heat flux generated by the temperature gradient $\boldsymbol{\nabla}T$, thus describing non-equilibrium phenomena. If only a locally small variation in the temperature is considered, the heat flux in terms of the phonon modes becomes [22]

$$\boldsymbol{Q} = \frac{1}{NV_0} \sum_{\boldsymbol{q},s} \hbar\omega_{\boldsymbol{q}s} \langle n_{\boldsymbol{q}s}(T)\rangle \boldsymbol{\nu}_{\boldsymbol{q}s} \; , \tag{2.3.2}$$

with the group velocity $\boldsymbol{\nu}_{\boldsymbol{q}s} = \nabla_{\boldsymbol{q}}\omega_{\boldsymbol{q}s}$ of the phonon, the energy of a phonon $\hbar\omega_{\boldsymbol{q}s}$ with average occupation $\langle n_{\boldsymbol{q}s}\rangle$, as derived in the harmonic approximation (see Sec. 2.2), the volume of the unit cell V_0 and N the number of unit cells. In the following, the temperature dependence of the distribution is not written down explicitly anymore for better readability. The symmetry of the phonon dispersion relation leads to an antisymmetry of the group velocity $\omega_{\boldsymbol{q}s} = \omega_{-\boldsymbol{q}s} \Rightarrow \boldsymbol{\nu}_{\boldsymbol{q}s} = -\boldsymbol{\nu}_{-\boldsymbol{q}s}$, so that in equilibrium with a symmetric occupation number $\langle n_{\boldsymbol{q}s}^0\rangle = \langle n_{-\boldsymbol{q}s}^0\rangle$ the average heat flux becomes zero. A net heat flux can only arise if the $\boldsymbol{q}$ symmetry of the phonon distribution is broken, $\langle n_{\boldsymbol{q}s}\rangle \neq \langle n_{-\boldsymbol{q}s}\rangle$. As the symmetrical Bose-Einstein distribution holds in the harmonic approximation, anharmonicity has to be taken into account to break the symmetry in the phonon distribution and allow for a total heat flux unequal to zero. The deviation of the distribution from the Bose-Einstein distribution is enforced through a mode dependent deviation $\eta_{\boldsymbol{q}s}$ which leads to the phonon distribution

$$\langle n_{\boldsymbol{q}s}\rangle = \frac{1}{\exp\left(\frac{\hbar\omega_{\boldsymbol{q}s}}{k_{\mathrm{B}}T} - \eta_{\boldsymbol{q}s}\right) - 1} = \langle n_{\boldsymbol{q}s}^0\rangle - \left.\frac{\partial\langle n_{\boldsymbol{q}s}\rangle}{\partial\eta_{\boldsymbol{q}s}}\right|_{\eta_{\boldsymbol{q}s}=0} \eta_{\boldsymbol{q}s} + \mathcal{O}(\eta_{\boldsymbol{q}s}^2) \; , \tag{2.3.3}$$

$$= \langle n_{\boldsymbol{q}s}^0\rangle + \eta_{\boldsymbol{q}s}\frac{k_{\mathrm{B}}T^2}{\hbar\omega_{\boldsymbol{q}s}}\frac{\partial\langle n_{\boldsymbol{q}s}^0\rangle}{\partial T} + \mathcal{O}(\eta_{\boldsymbol{q}s}^2) \; . \tag{2.3.4}$$

The Taylor expansion is truncated after the first order as the deviation from the equilibrium is considered to be small. The non-equilibrium phonon distribution should fulfill the linearized

2. Theoretical Background

Boltzmann equation in steady state [3]

$$-\boldsymbol{\nu_{qs}}\boldsymbol{\nabla}T\frac{\partial\langle n_{qs}\rangle}{\partial T} = -\left.\frac{\partial\langle n_{qs}\rangle}{\partial t}\right|_{\text{scattering}} . \tag{2.3.5}$$

The left hand side gives the diffusion of the distribution due to the applied temperature gradient. The right hand side gives the change of the distribution due to scattering, so that the total rate of change of the phonon distribution vanishes. In general the right hand side is complicated but it can be solved by applying the so called *single mode relaxation time* approximation (RTA) . This approximation assumes for the relaxation time of a phonon that all other phonons follow the equilibrium distribution ($\eta_{q's'} = 0$ for $\boldsymbol{q's'} \neq \boldsymbol{qs}$)

$$\left.\frac{\partial\langle n_{qs}\rangle}{\partial t}\right|_{\text{scattering}} \approx \frac{\langle n_{qs}\rangle - \langle n_{qs}^0\rangle}{\tau_{qs}} \approx \frac{\eta_{qs}}{\tau_{qs}}\frac{k_{\mathrm{B}}T^2}{\hbar\omega_{qs}}\frac{\partial\langle n_{qs}^0\rangle}{\partial T} . \tag{2.3.6}$$

In the last step, the truncated Eq. (2.3.4) was plugged in and the relaxation time τ_{qs} was introduced. With Eq. (2.3.5) and (2.3.6), an expression for η_{qs} can be found which is inserted into the phonon occupation number and then into Eq. (2.3.2)

$$\boldsymbol{Q} = -\frac{1}{V_0}\sum_{\boldsymbol{q},s}\frac{(\hbar\omega_{qs})^2}{k_{\mathrm{B}}T^2}\tau_{qs}\langle n_{qs}^0\rangle(\langle n_{qs}^0\rangle + 1)\boldsymbol{\nu_{qs}}\otimes\boldsymbol{\nu_{qs}}\boldsymbol{\nabla}T . \tag{2.3.7}$$

Comparing this to the Fourier's law, Eq. (2.3.1), yields for the thermal conductivity

$$\underline{\underline{\boldsymbol{\kappa}}} = \frac{1}{V_0}\sum_{\boldsymbol{q},s}\frac{(\hbar\omega_{qs})^2}{k_{\mathrm{B}}T^2}\tau_{qs}\langle n_{qs}^0\rangle(\langle n_{qs}^0\rangle + 1)\boldsymbol{\nu_{qs}}\otimes\boldsymbol{\nu_{qs}} \tag{2.3.8}$$

$$= \frac{1}{V_0}\sum_{\boldsymbol{q},s}\tau_{qs}c_{qs}\nu_{qs}\otimes\nu_{qs}. \tag{2.3.9}$$

To obtain a scalar quantity, one takes $\kappa = \frac{1}{3}\mathrm{Tr}(\underline{\underline{\boldsymbol{\kappa}}})$. The phonon mode specific heat c_{qs}, which is defined by Eq. (2.2.21), and the group velocity $\boldsymbol{\nu_{qs}}$ can already be calculated in the harmonic approximation.

Because of Matthiessen's rule the inverse of the total relaxation time can be split into multiple parts due to boundary scattering, mass defect scattering and phonon-phonon scattering. Boundary scattering can be neglected as we assume an infinite size crystal. Mass defect scattering will be neglected for the further derivation as well as the crystal is considered to be perfect without mass defects. Within these restrictions the relaxation time is approximated with the life time of a phonon. However, in the harmonic approximation the phonon life time is infinite because no scattering processes are limiting it and its mean free path is infinite. If anharmonicity is taken into account, the phonon life time can be obtained via the imaginary part of the self-energy Γ_{qs}

$$\tau_{qs} = \frac{1}{2\Gamma_{qs}} . \tag{2.3.10}$$

Where $\Gamma_{\boldsymbol{q}s}$ can be expressed through [20]

$$
\begin{aligned}
\Gamma_{\boldsymbol{q}s} = \frac{18\pi}{\hbar^2} \sum_{\boldsymbol{q}'s',\boldsymbol{q}''s''} & |\Psi_{s,s',s''}(\boldsymbol{q},\boldsymbol{q}',\boldsymbol{q}'')|^2 \\
\times \Big\{ & \left(\langle n^0_{\boldsymbol{q}'s'} \rangle + \langle n^0_{\boldsymbol{q}''s''} \rangle + 1 \right) \delta(\omega_{\boldsymbol{q}s} - \omega_{\boldsymbol{q}'s'} - \omega_{\boldsymbol{q}''s''}) \\
+ & \left(\langle n^0_{\boldsymbol{q}'s'} \rangle - \langle n^0_{\boldsymbol{q}''s''} \rangle \right) \left[\delta(\omega_{\boldsymbol{q}s} + \omega_{\boldsymbol{q}'s'} - \omega_{\boldsymbol{q}''s''}) - \delta(\omega_{\boldsymbol{q}s} - \omega_{\boldsymbol{q}'s'} + \omega_{\boldsymbol{q}''s''}) \right] \Big\} \,,
\end{aligned}
\tag{2.3.11}
$$

if only third order anharmonicity is taken into account, with the Fourier transformed third order force constants

$$
\begin{aligned}
\Psi_{s,s',s''}(\boldsymbol{q},\boldsymbol{q}',\boldsymbol{q}'') = \frac{1}{3!} \left(\frac{\hbar}{2N} \right)^{\frac{3}{2}} & \sqrt{\frac{1}{\omega_{\boldsymbol{q}s}\omega_{\boldsymbol{q}'s'}\omega_{\boldsymbol{q}''s''}}} \\
\times \sum_{IJK} \sum_{\alpha\beta\gamma} \Psi_{IJK,\alpha\beta\gamma} & \sqrt{\frac{1}{M_I M_J M_K}} e^{i\boldsymbol{q}\boldsymbol{R}_I} e^{i\boldsymbol{q}'\boldsymbol{R}_J} e^{i\boldsymbol{q}''\boldsymbol{R}_K} \\
\times e_{Is\alpha}(\boldsymbol{q}) & e_{Js'\beta}(\boldsymbol{q}') e_{Ks''\gamma}(\boldsymbol{q}'') \,.
\end{aligned}
\tag{2.3.12}
$$

The eigenvectors $e_{Is\alpha}(\boldsymbol{q})$ are obtained from the dynamical matrix in Eq. (2.2.12). Finally, this force constants $\Psi_{IJK,\alpha\beta\gamma}$ can be obtained through force calculations as explained in Sec. 2.1.1 and the finite difference method.

In the high temperature limit the major contribution of the phonons have the energy $\hbar\omega_{\mathrm{max}}$. If assuming this holds for all phonons, the phonon distribution becomes proportional to the temperature T and the relaxation time proportional to T^{-1} which yields for the thermal conductivity [4]

$$
\kappa \propto \frac{1}{T} \,.
\tag{2.3.13}
$$

2.4. Thermal Expansion

Another anharmonic effect is the lattice expansion with respect to the temperature, which is simply defined as the temperature derivative of the volume V

$$
\alpha(T) = \frac{1}{V} \left. \frac{\partial V}{\partial T} \right|_P
\tag{2.4.1}
$$

$$
\beta(T) = \frac{1}{L} \left. \frac{\partial L}{\partial T} \right|_P = \frac{\alpha(T)}{3}.
\tag{2.4.2}
$$

The last equation only holds for isotropic crystals with the length L. In a harmonic potential as treated in Sec. 2.2, there is no thermal expansion because the expectation value of the position does not change with temperature due to the symmetry of the potential. However, to obtain the expectation value of the position one actually has to minimize the Helmholtz free energy F.

In the quasi harmonic approximation it is assumed that the harmonic approximation holds for every volume. The free energy can be approximated in the way that $F \approx E_{\mathrm{el}} + F^{\mathrm{vib}}_{\mathrm{ha}}(T)$, with the the vibrational free energy $F^{\mathrm{vib}}_{\mathrm{ha}}(T)$ of the nuclei and the electronic energy E_{el}. So the free energy is a function of the volume and can be minimized with respect to this

parameter. For the minimization the Birch-Murnaghan equation for the energy is applied to have a direct representation of lattice properties [23]

$$E(V) = E_0 + \frac{9B_0V_0}{16} \left\{ \left[\left(\frac{V_0}{V} \right)^{\frac{2}{3}} - 1 \right]^3 B_0' + \left[\left(\frac{V_0}{V} \right)^{\frac{2}{3}} - 1 \right]^2 \left[6 - 4 \left(\frac{V_0}{V} \right)^{\frac{2}{3}} \right] \right\} \; . \quad (2.4.3)$$

Here, B_0 is the bulk modulus, B_0' its first derivative and the equilibrium volume V_0. This can be done for all temperatures and so the temperature derivative of the volume can be accessed. This procedure is illustrated in Fig. 2.1. This equation can be generalized to include more degrees of freedom in the lattice parameters and this generalization for one more degree of freedom can be found in App. B.
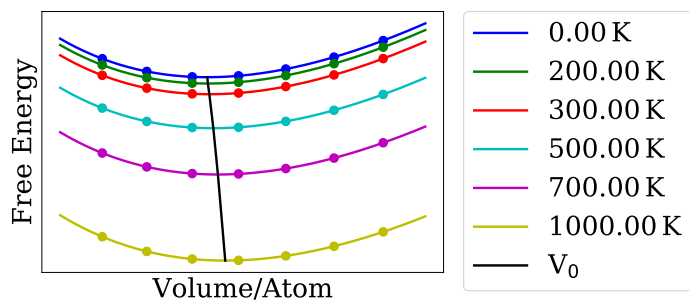

Figure 2.1.: Quasi Harmonic approximation. Dots give the different calculated points, which were plotted. The black line gives the equilibrium position at the given temperature, which increases with rising temperature.

3. The Computational Setup: A Case Study of Silicon

The first-principles calculations with the all-electron, full-potential electronic structure density-functional theory code *FHI-aims* determine the electronic structure of the systems, so the electron density and from that the forces on the atoms [8]. The relevant physical approximations of the exchange-correlation functional and the relevant numerical parameters, the number of integration points in the reciprocal space, the accuracies of the density and the forces, and the used basis functions, must be tested. To calculate harmonic properties via force constants, the functionalities of *phonopy* are used [9]. This algorithm utilizes the finite difference and supercell approaches. The relevant parameters in this model are the displacement distance and the supercell size. To calculate thermal conductivities via force constants, the functionalities of *phono3py* are used [10]. It uses the same utilities as above and the same parameters are investigated. A special focus must be placed on the force accuracy as this has a considerable influence on the thermal conductivity. In the following, these parameters will be checked on the case of diamond structured silicon. If nothing else is mentioned *light* basis sets as implemented in *FHI-aims* are used.

3.1. Settings for the Force Calculations

Force calculations and calculations of the equilibrium structure for $0\,\mathrm{K}$, neglecting zero point vibrations, do not require any phonon calculations and are performed in *FHI-aims*. Therefore, these settings are tested first. Relaxations of the structure were done with *tight* basis sets.

3.1.1. Convergence of the Reciprocal Space Sampling Grid

The total energy and the lattice constant converge depending on the number of integration points in every direction. Therefore, the structure is relaxed for up to 40 integration points in every direction. In Fig. 3.1, the convergence over the number of integration points is shown. The deviation of the lattice constant to its converged value with 40 integration points in every direction is already zero for 7 integration points in every direction. The deviation of the total energy is below $10\,\mathrm{meV}$ per atom, which is "chemical accuracy", at 3 integration points.

3.1.2. Influence of the Exchange-Correlation Functional on the Lattice Constant

As explained in Sec. 2.1.1 one has to approximate the exchange-correlation functional. The lattice constant is evaluated for some of the most common functionals. In Fig. 3.2, a comparison is shown. The experimental value for the lattice constant $a = 5.43\,\text{Å}$ [24] is shown
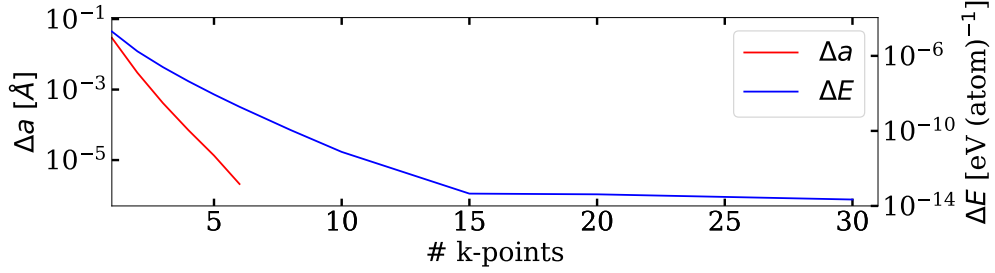
Figure 3.1.: Convergence of the integration grid, with same number of integration points in every direction. (Red) Deviation of the lattice constant a from its converged value at a density of integration points (k-points) of 40. Zero from 6 points on. (Blue) Deviation of the total energy of the conventional unit cell E from its value with the highest number of k-points (40).

(red line). The bars represent the lattice constants a calculated with the *PW-LDA* [25] approximation, the GGA approximations *PBE* [15] and *PBEsol* [16], the hybrid functional *PBE0* [26] and the pure Hartree-Fock (*HF*) approximation. In the hybrid functional *PBE0*, *PBE* exchange-correlation and Hartree-Fock exchange are mixed together. *PBEsol* and the computationally costly *PBE0* deviate the least from the experimental lattice constant. Additionally, the deviation of the lattice constant calculated with *PBE* and *PBEsol* were compared for all 35 examined materials, which yielded a smaller root mean square for *PBEsol* compared to the experiment. Please note that zero-point vibrations still slightly alter the equilibrium lattice constants at 0K, as discussed later in the context of thermal expansion. Nonetheless, root mean square errors for *PBEsol* are $\Delta a_{\mathrm{cubic}} = 0.02\,\text{Å}$, $\Delta a_{\mathrm{wurtzite}} = 0.008\,\text{Å}$ and $\Delta c_{\mathrm{wurtzite}} = 0.011\,\text{Å}$. Consequently all further calculations were done with *PBEsol*.
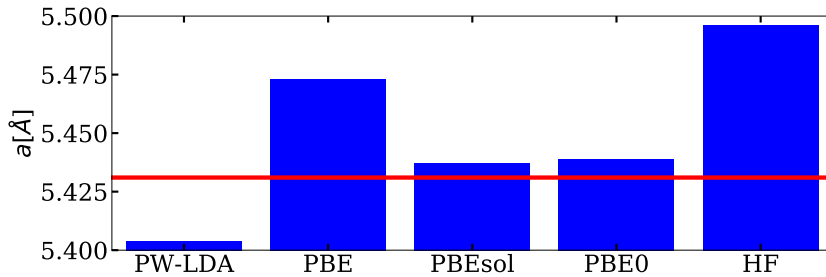
Figure 3.2.: Lattice constant with different approximations of the exchange-correlation functional. The line gives the experimental value of the lattice constant [24].

3.1.3. Influence of the Basis Set on the Lattice Constant

In *FHI-aims*, default basis sets and numerical presets are provided to reach different levels of accuracy. *Light* basis sets yielded $a = 5.45\,\text{Å}$ and *tight* and *really tight* basis sets yielded $a = 5.44\,\text{Å}$ for the lattice constant. The influence on the lattice constant is thus around 0.2%.

3.2. Settings for the Second-Order Force Constants

Since the forces do not follow a variational principle themselves, they typically require more accurate numerical settings to converge than the densities and the lattice constants. Consequently, the forces converge differently compared to the density and their convergence behaviour has to be investigated separately. Second-order force constants are calculated with *phonopy* from the forces calculated in a supercell. A not converged, i.e., large enough, supercell size gives an error, as it is a truncation of the sum in Eq. 2.2.11. This was explicitly investigated. Similarly, the displacement distance for the finite difference calculations was doubled and the force accuracies were tuned up from $10^{-4} \, \mathrm{eV\mathring{A}}^{-1}$. None showed a significant influence on the harmonic properties.

3.2.1. Influence of the Supercell Size on the Phonon Band Structure
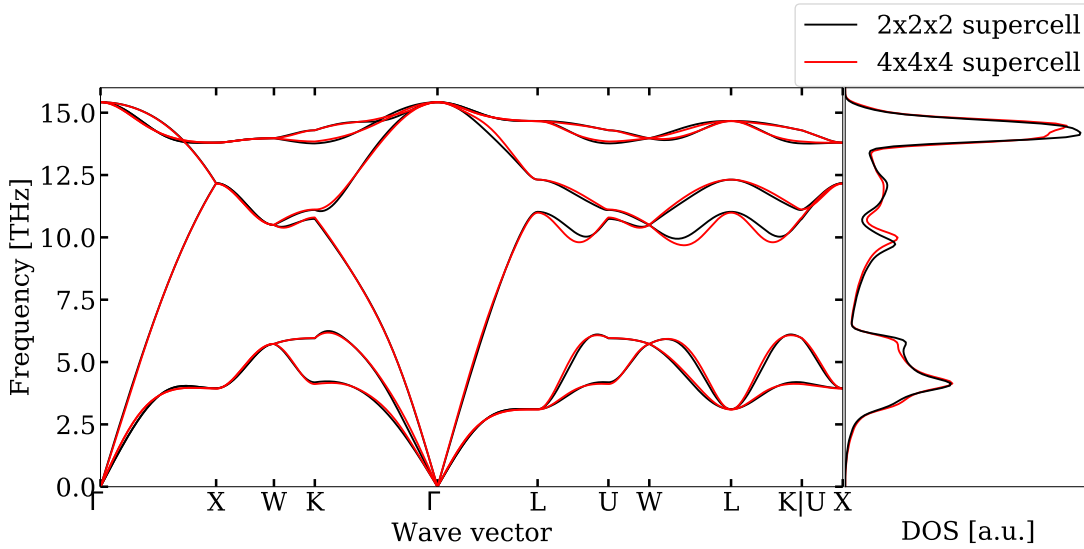
Figure 3.3.: *Left:* Calculated phonon band structure for diamond silicon for a $2 \times 2 \times 2$ (black) and $4 \times 4 \times 4$ (red) supercell. *Right:* Calculated density of states for the same structure with the same settings.

A bigger supercell should give better results as also longer ranging forces are calculated and the force constants are built upon that. The supercell was tuned between $2 \times 2 \times 2$ and $4 \times 4 \times 4$ of the conventional unit cell. In Fig. 3.3 two phonon band structures are shown together with the density of states which deviated as well according to the supercell size. The $4 \times 4 \times 4$ supercell phonon band structures shows small deviations from the $2 \times 2 \times 2$ supercell. The biggest deviations can be observed between 10 and 11 THz at the W,L and K point in the third band. The $3 \times 3 \times 3$ phonon band structure gave the same results as the $4 \times 4 \times 4$ phonon band structure, so that convergence was reached.

3.3. Settings for the Third-Order Force Constants

Third-order force constants computed with *phono3py* are even more sensible to numerical noise, given that this relatively small quantities are obtained from a second-order finite difference. Accordingly, not only the supercell size but also the force accuracy and the displacement distance are important to check. Generally, the size of the supercell can be smaller than in the case of harmonic calculations, as the third-order forces are typically of shorter range.

3.3.1. Influence of the Displacement Distance on the Thermal Conductivity

For a $3 \times 3 \times 3$ supercell of the conventional cell with a sampling mesh of the reciprocal space in the primitive unit cell of $10 \times 10 \times 10$, the thermal conductivity was calculated depending on the displacement distance. The thermal conductivity in these settings for different displacements can be seen on the left side of Fig. 3.4. The thermal conductivity deviates for displacement distances between $0.03\,\text{Å}$ and $0.09\,\text{Å}$ by $5\,\text{Wm}^{-1}\text{K}^{-1}$, which corresponds to a relative error of below 5%. For the remaining calculations the default displacement distance of $0.03\,\text{Å}$ is chosen as it allows for comparison with Ref. [10]. The same test was done for a $2 \times 2 \times 2$ supercell, which showed the same dependence of the thermal conductivity on the displacement distance.
The influence of the displacement was probed with more accurate calculated forces, using a *tight* basis sets. The behaviour is similar, beside the fact that even at smaller displacement distances the obtained values did not deviate more than $5\,\text{Wm}^{-1}\text{K}^{-1}$ from the rest. Calculating better converged forces thus allows for a smaller displacement which consequently allows for a better approximation of the derivative of the force and so the force constants. To check the importance of the displacement distance, the calculations were repeated for gallium arsenide. The thermal conductivity of gallium arsenide showed smaller absolute deviations, but larger relative deviation in the probed range than silicon, which is understandable from its smaller thermal conductivity.

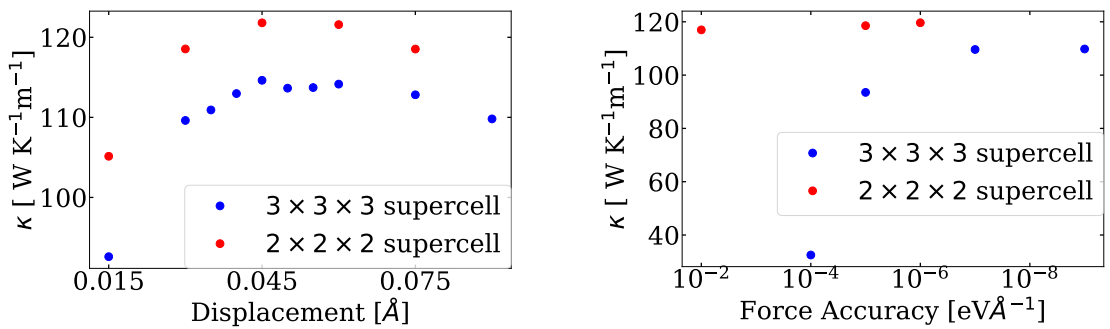### 3.3.2. Influence of the Force Accuracy on the Thermal Conductivity

Figure 3.4.: *Left:* Influence of the displacement distance on the thermal conductivity. *Right:* Influence of the accuracy of the forces on the thermal conductivity.

As the thermal conductivity is highly sensitive on the accuracy of the forces, different force

accuracies were tested. To examine this influence thermal conductivities were calculated in the same settings as above. The force accuracy was tuned from $10^{-4}\,\text{eV\AA}^{-1}$ to $10^{-9}\,\text{eV\AA}^{-1}$. In Fig. 3.4 one can see the influence of the forces accuracy on the thermal conductivity. Convergence seems to be reached for a force accuracy of $10^{-7}\,\text{eV\AA}^{-1}$. The same convergence test for a $2 \times 2 \times 2$ supercell yielded nearly no deviation up from $10^{-2}\,\text{eV\AA}^{-1}$.

3.3.3. Influence of the Basis Set on the Thermal Conductivity

The accuracy of the forces depend on the basis sets. In the same manner as above thermal conductivities were calculated for different basis sets as implemented in *FHI-aims*. The supercell was set to $2 \times 2 \times 2$ of the conventional cell because calculation with *tight* and *really tight* basis sets are computational very demanding. The force accuracy was set to $10^{-5}\,\text{eV\AA}^{-1}$ as this tends to be a smaller issue in smaller supercells. The basis set for the relaxation of the geometry and the basis set for the force calculation were treated separately. Note that the chosen settings are not the converged settings, so that the experimental value is not reached. In Tab. 3.1 the thermal conductivity is listed over the different applied parameters. One can see that more accurate forces tend to give higher thermal conductivities which results in a 8% lower thermal conductivity of the *light* basis set calculation compared to the tightest ones. If the geometry is calculated with *tight* basis sets first, the thermal conductivity only deviates 6% from the tightest value. The geometry in *tight* and *really tight* did not deviate at all. Even though a tighter basis set gives better results, they are computational more demanding, so that force calculations in the *light* basis set were standard. The relaxation were done with *tight* basis sets. This choice of basis sets yields an error for the thermal conductivity which is material dependent as one can see in App. F.

Table 3.1.: Influence of different basis sets as implemented in *FHI-aims* on the thermal conductivity. The experimental value is for isotope purified silicon.

Relaxation basis set	Force calculation basis set	$\kappa[\frac{\text{W}}{\text{mK}}]$
light	*light*	116.41
light	*tight*	125.78
tight	*light*	118.54
tight	*tight*	123.88
tight	*really tight*	126.39
Experiment [27]		156.4

To summarize, we find that the calculation of third-order force constants typically requires much more accurate numerical settings than typically used in electronic-structure theory calculations. This is not too surprising, given that much smaller quantities need to be assessed in a second-order finite difference approach. Still, the fact that even individual numerical parameters can alter the resulting thermal conductivities by up to 10% is alarming, given that these numerical uncertainties have so far not yet been systematically discussed in literature.

4. Results

4.1. The Computational Settings

In line with the above discussed tests, the computational settings were chosen as: The PBEsol exchange correlation functional was used. The electron density was calculated with a precision of 10^{-6} eV and the forces with a precision of 10^{-5} eVÅ^{-1}. The reciprocal space of the conventional cell was sampled with $8 \times 8 \times 8$ and $10 \times 10 \times 9$ grids for the zincblende and wurtzite structures respectively.

For second-order force constant calculations the displacement distance was chosen to 0.01 Å and for the third-order force constant calculations 0.03 Å. For calculations of the second-order force constants and the harmonic properties with *phonopy* the supercell for zincblende/ diamond and wurtzite type were $4 \times 4 \times 4$ (512 atoms) and $5 \times 5 \times 3$ (300 atoms) of the conventional cell respectively. The reciprocal lattice for the zincblende/diamond supercell was sampled in $2 \times 2 \times 2$ grid and for the wurtzite one in $2 \times 2 \times 3$.

Third-order force constants were calculated with *phono3py* in a $2 \times 2 \times 2$ (64 atoms) and a $3 \times 3 \times 2$ (72 atoms) supercell for zincblende/diamond and wurtzite respectively. For zincblende the reciprocal space was sampled in a $4 \times 4 \times 4$ grid and for wurtzite in a $3 \times 3 \times 4$ grid. The thermal conductivity was calculated with a $20 \times 20 \times 20$ sampling mesh in the reciprocal space of the primitive unit cell.

4.2. Diamond Silicon

Silicon is the second most abundant element in earth's crust and an important semiconductor. Its diamond structured phase is the starting point for the discussion of thermal expansion and conductivity in this work.

4.2.1. Harmonic Properties

In Sec. 2.2, the harmonic approximation and the possibility to predict certain properties within it was discussed.

The phonon band structure ω_{qs} of silicon is displayed in Fig. 3.3 along the path Γ, X, W, K, Γ, L, U, W, L, K and U, X, which can be found in App. A. In total there are six phonon bands in this crystal due to the three dimensions and the two atoms in the primitive unit cell. The three lower ones are acoustic modes and the three upper ones are optical modes. In Fig. 3.3 the density of states is plotted over the frequency. The relation between band flatness and high densities of states can be observed for example at 4 THz or 14 THz. As discussed in Sec. 2.2, the harmonic approximation allows for the evaluation of the Helmholtz free energy F, the entropy S and the heat capacity C_V. In Fig. 4.1, these properties are shown. In the high temperature limit the heat capacity approaches the classical Dulong-Petit value (dashed line).
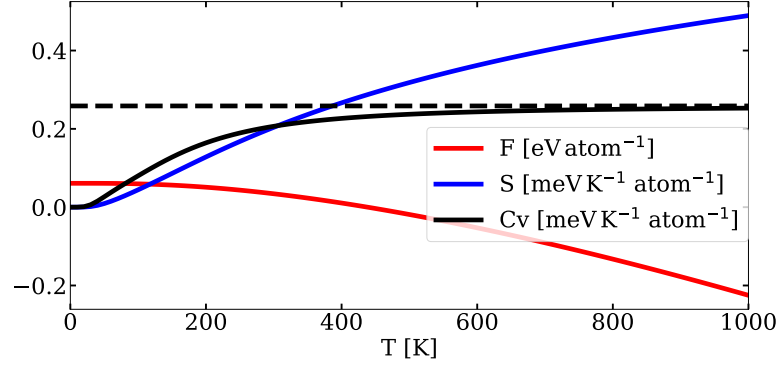
Figure 4.1.: Calculated Helmholtz free energy, entropy and heat capacity over the temperature. The dashed line gives the Dulong-Petit limit of the heat capacity.

4.2.2. Thermal Expansion

The thermal expansion was calculated in the quasi harmonic approximation as briefly explained in Sec. 2.4. The linear thermal expansion coefficient for diamond silicon is shown in Fig. 4.2. The calculated thermal expansion is negative around $100\,\text{K}$. This matches with experiment and previous theoretical discussion [28, 29]. This property is typical for zincblende semiconductors. The calculated linear thermal expansion at $300\,\text{K}$ is $2.87 \cdot 10^{-6}\,\text{K}^{-1}$. This compares well with the experimental value of $2.59 \cdot 10^{-6}\,\text{K}^{-1}$ [30].
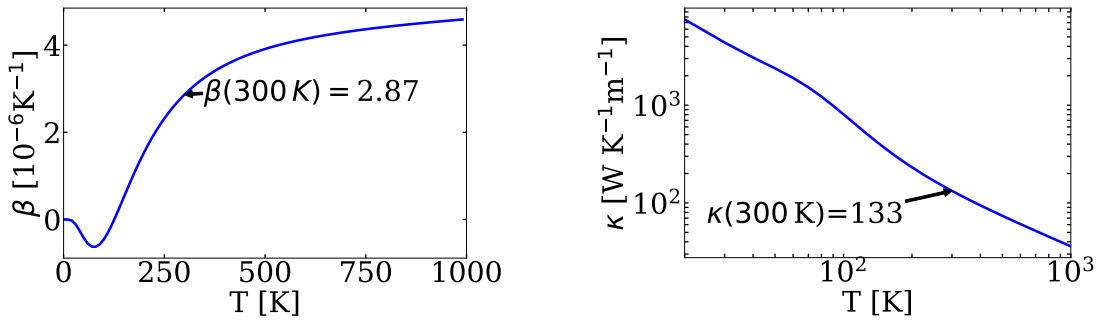
Figure 4.2.: *Left:* Linear thermal expansion coefficient β over the temperature. *Right:* Calculated thermal conductivity κ of isotropic diamond silicon. The calculation was done including mass defect scattering effects for the $0\,\text{K}$ geometry.

4.2.3. Thermal Conductivity

The thermal conductivity was calculated using *phono3py* with and without inclusion of mass defect scattering for the relaxation time. A calculation for the $0\,\text{K}$ geometry and one with a adjusted lattice were made including mass defect scattering. The expansion was obtained through the thermal expansion calculations from above. For all calculations the obtained force constants were symmetrized due to the symmetry of the lattice. The thermal

Table 4.1.: Thermal conductivity of silicon diamond for different settings at 300 K. The experimental value is for a natural composition of silicon.

Settings	κ $[\frac{W}{Km}]$
Without isotope effect	141.22 ± 6.50
With isotope effect	132.86 ± 6.17
With isotope effect and **adjusted lattice**	124.63 ± 3.76
Experiment	148 [31]

conductivity can be seen in Fig. 4.2 on the right side including the mass defect effects for the 0 K geometry. The thermal conductivities for the different calculations can be found in Tab. 4.1. The error values are obtained from comparing the calculation with symmetrisation and without symmetrisation of the force constants. This is a measure for the quality of the force constants [10].

All calculated conductivities are smaller than the experimental. One reason could be the chosen basis set (see Sec. 3.3.3).

4.3. Thermal Expansion
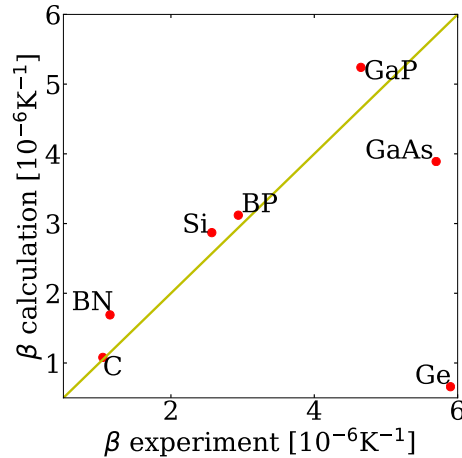
Figure 4.3.: Comparison of the calculated and experimental linear thermal expansion coefficients β at 300 K for the cubic materials. The line (yellow) gives the matching line of experiment and calculation.

Thermal expansion coefficients were calculated for group IV and group III-V compound semiconductors in zincblende/diamond and wurtzite structure within the quasi harmonic approximation. For the cubic materials the Birch-Murnaghan equation of state was used to minimize the Helmholtz free energy. For the wurtzite materials a two dimensional Birch-Murnaghan was applied, which takes the ratio between the two different lattice constants as an additional degree of freedom (see App. B). From this, direction dependent thermal

expansion coefficients were calculated. In the following, x defines the in plane direction and z the perpendicular one to the plane. The calculations were performed in the temperature range between $0\,\mathrm{K}$ and $1000\,\mathrm{K}$. A comparison between the calculated linear thermal expansion coefficients at $300\,\mathrm{K}$ with the corresponding experimental values is illustrated in Fig. 4.3. The values can be found in App. C. In some cases, the calculations deviate significantly with respect to the experimental value. Please note that germanium is a special case, since it is a metal in the PBEsol approximation, even though it is a semiconductor in reality. For gallium arsenide and boron nitride the deviations to the experiment are around 40% but for the discussed case of silicon, carbon, boron phosphide and gallium phosphide these deviations smaller than 13%. For carbon only 3% deviation to the experimental value was observed. The RMSE of the linear thermal expansion compared to the experimental data is $2.1 \cdot 10^{-6}\,\mathrm{K}^{-1}$ and without germanium $0.8 \cdot 10^{-6}\,\mathrm{K}^{-1}$. For aluminium arsenide the quasi harmonic approximation predicts a negative thermal expansion over the whole temperature range.

The quasi harmonic approximation can thus give reasonable qualitative and quantitative results, but one should not rely blindly on it. A discussion in this spirit can be found in Ref. [32]. However, for most of the zincblende structures a negative thermal expansion was found in the low temperature range which compares well to experiment. An explanation and further discussion of this behaviour of zincblende semiconductors can be found in Ref. [29].

4.4. Thermal Conductivity

The thermal conductivity for 35 materials was obtained by computing second- and third-order force constants from supercells with displacements created by *phono3py*, using *FHI-aims* with the in Sec. 4.1 discussed settings. The post processing was performed with *phono3py* using a sampling grid of the reciprocal space of the primitive unit cell of $20 \times 20 \times 20$.

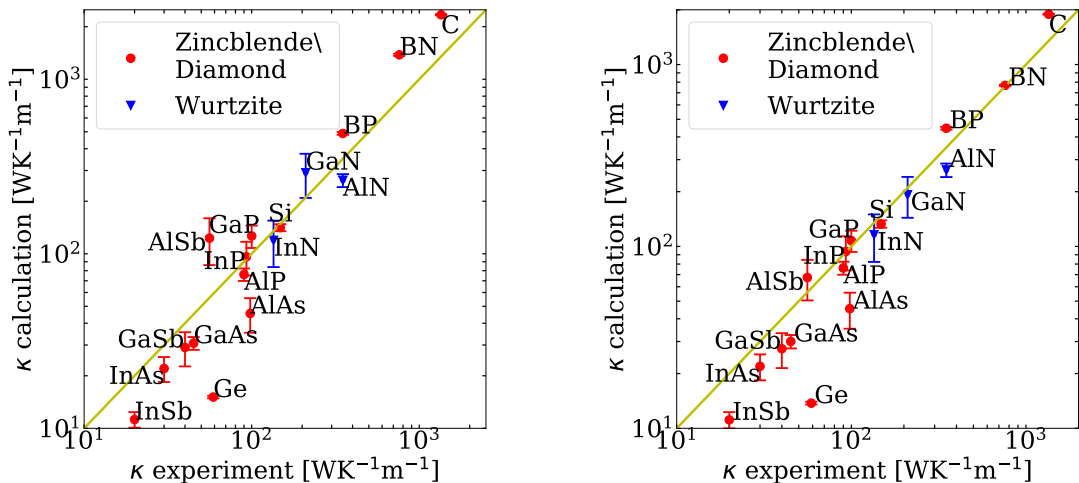Figure 4.4.: Comparison of the calculated thermal conductivity at $300\,\mathrm{K}$ with the experimental values. *Left:* Without isotope scattering. *Right:* With isotope scattering. The yellow line gives the conformance of experimental and calculated value.

Firstly, the thermal conductivity was calculated in the relaxation time approximation with neglected mass defect scattering. In App. D the thermal conductivities are listed for the zincblende/diamond and wurtzite structures at 300 K. On the left side of Fig. 4.4 one can see a comparison of the calculated values with the experimental ones. For the comparison of the wurtzite the scalar thermal conductivity was used ($\kappa = \mathrm{Tr}(\underline{\underline{\kappa}})/3$). The values deviate from the line of conformance with experiment but the right trend was captured. The thermal conductivities are for 9 cubic materials between 10-100 $\mathrm{Wm^{-1}K^{-1}}$ for 8 between 100-1000 $\mathrm{Wm^{-1}K^{-1}}$ and for 3 above 1000 $\mathrm{Wm^{-1}K^{-1}}$. The corresponding wurtzite type materials follow the same distribution.

Note that *PBEsol* still is not a good functional to discuss germanium as already mentioned above. This leads to an unreliable thermal conductivity for germanium. Moreover, carbon deviates approximately 1000 $\mathrm{WK^{-1}m^{-1}}$ from its experimental value. Carbon has a high thermal conductivity due to a long relaxation time and so a long mean free path of the phonons. Consequently, other scattering effects (e.g. boundary and mass defect scattering) may be more important for the real thermal conductivity. The RMSE to experiment was determined to be 316.2 $\mathrm{WK^{-1}m^{-1}}$ for the cubic materials, 69.2 $\mathrm{WK^{-1}m^{-1}}$ for the wurtzite materials and 288.4 $\mathrm{WK^{-1}m^{-1}}$ for the combination of both. This exceeds most of the actually computed thermal conductivities, so that an improvement of the calculations is needed.

Mass defect scattering was then taken into account as the experimental values are for natural compositions of the materials and not isotopic purified ones. In Tab. 4.2 the thermal conductivities at 300 K are shown with the inclusion of this. The thermal conductivities are for 10 cubic materials between 10-100 $\mathrm{Wm^{-1}K^{-1}}$, for 8 between 100-1000 $\mathrm{Wm^{-1}K^{-1}}$ and for 2 above 1000 $\mathrm{Wm^{-1}K^{-1}}$. The illustrated comparison of experiment and calculations can be found on the right hand side of Fig. 4.4. For example, the calculated value of boron nitride shifted to a lower value and nearly matches the experimental value. In general, the inclusion of the treatment of mass defects leads to decreasing thermal conductivities because an additional scattering term is included. Moreover, for some low thermal conducting materials the calculations were done with more accurate calculated forces as well. Therefore *tight* basis sets were used. The deviations range from 0.2% up to 54% and are material dependent. The results can be found in App. F.

The thermal conductivities compare well to Ref. [10]. However, the RMSE to the experiment is 148.1 $\mathrm{WK^{-1}m^{-1}}$ for cubic materials, 52.3 $\mathrm{WK^{-1}m^{-1}}$ for wurtzite materials and 134.4 $\mathrm{WK^{-1}m^{-1}}$ for the combination of both. Even though this is a drastic decrease in the RMSE, the RMSE still exceeds many of the values. However, it was checked if only the better conformance of a some high thermal conductivity materials lead to this decrease. This was not the case as the RMSE also decrease excluding thermal conductivities above 100 $\mathrm{WK^{-1}m^{-1}}$.

The mass does not influence the thermal conductivity only by mass defect scattering but generally there is a trend that with increasing reduced mass the thermal conductivity declines. In Fig. 4.5 the thermal conductivity was plotted over the reduced mass, which was equated for wurtzite and zincblende

$$\mu = \frac{m_1 m_2}{m_1 + m_2} \; . \tag{4.4.1}$$

Table 4.2.: Calculated thermal conductivities including mass defect scattering, as treated in *phono3py*, at $300\,\text{K}$ in W K^{-1}m^{-1}. Cubic means zincblende and diamond structure. Experimental values are for $300\,\text{K}$ as well.

	Cubic structure		Wurtzite structure		
	κ	Exp	κ_x	κ_z	Exp
C	1890.1 ± 10.0	1350.0 [a]	-	-	-
Si	132.9 ± 6.2	148.0 [a]	-	-	-
Ge	13.7 ± 0.2	59.0 [a]	-	-	-
Sn	13.5 ± 1.1	-	-	-	-
BN	768.6 ± 6.5	760.0 [b]	622.6 ± 4.9	623.5 ± 17.9	-
BP	446.6 ± 7.4	350.0 [b]	395.5 ± 6.4	329.2 ± 63.3	-
BAs	1236.7 ± 45.0	-	1108.4 ± 117.9	955.7 ± 191.7	-
BSb	371.8 ± 26.2	-	-	-	-
AlN	268.8 ± 8.1	-	263.1 ± 20.3	263.2 ± 26.6	350.0 [b]
AlP	76.1 ± 6.3	90.0 [c]	64.3 ± 5.9	65.9 ± 8.1	-
AlAs	45.5 ± 10.2	98.0 [b]	47.2 ± 13.7	54.3 ± 12.4	-
AlSb	67.4 ± 16.9	56.0 [b]	39.7 ± 15.4	40.7 ± 14.6	-
GaN	147.4 ± 58.4	-	187.5 ± 45.9	202.4 ± 44.2	210.0 [b]
GaP	107.6 ± 14.4	100.0 [b]	102.5 ± 37.3	98.2 ± 38.8	-
GaAs	30.0 ± 2.5	45.0 [b]	25.7 ± 10.3	27.8 ± 9.5	-
GaSb	27.4 ± 6.0	40.0 [b]	17.0 ± 9.6	17.5 ± 9.7	-
InN	129.5 ± 19.1	-	111.5 ± 28.4	125.3 ± 35.7	135.0 [d]
InP	93.8 ± 19.9	93.0 [b]	37.7 ± 21.5	47.0 ± 23.5	-
InAs	21.9 ± 3.6	30.0 [b]	16.0 ± 10.2	17.2 ± 10.1	-
InSb	11.1 ± 1.1	20.0 [b]	7.7 ± 4.4	9.0 ± 4.1	-

[a] Ref. [31]
[b] Ref. [33]
[c] Ref. [34]
[d] Ref. [35]

As the phonon frequency is calculated from the dynamical matrix, which scales approximately with μ^{-1} (Eq. (2.2.5)), the phonon frequency should show the same behaviour. With its quadratic influence on the thermal conductivity the same should scale with μ^{-2} (Eq. (2.3.8)). The fit $\kappa = a \cdot \mu^b$ with $b = -1.98$ is in good agreement with this predicted dependency.

Lastly, the influence of the lattice size on the thermal conductivity was examined. For the wurtzite types the influence of the lattice size on the thermal conductivity can be directly seen if one has a look a the direction dependent thermal conductivity divided by the corresponding lattice constant. For both the ratio is nearly equal. In App. E this was illustrated. For the cubic materials the unit cells were expanded due to the calculated thermal expansions. The calculated values can be found in App. F. There are still two materials above $1000\,\text{WK}^{-1}\text{m}^{-1}$, but only 7 between 100-1000 $\text{WK}^{-1}\text{m}^{-1}$ and 11 below $100\,\text{WK}^{-1}\text{m}^{-1}$. Overall the thermal conductivity decreased compared to the other calculations.
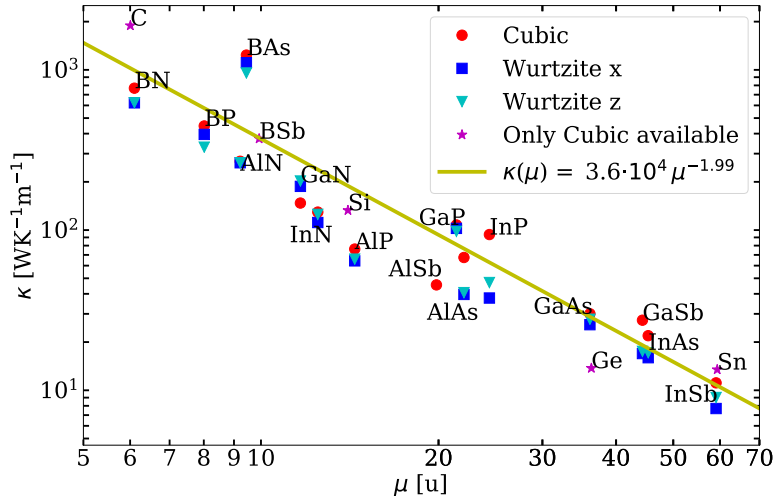
Figure 4.5.: Thermal conductivity plotted over the reduced mass μ. The yellow line gives a fit to $\kappa = a \cdot \mu^b$.

The RMSE in this calculation decreased further to $70.2\,\mathrm{WK^{-1}m^{-1}}$. This means that RMSE can be brought down to less than a fourth of the starting value with neglegence of mass defect scattering. This leads to the conclusion that when calculating thermal conductivities one should always have a look at the lattice and its actual size at the given temperature.

Additionally, for gallium phosphide, with a high thermal expansion, the whole temperature dependence of the thermal conductivity was calculated. Therefore every $100\,\mathrm{K}$ from $0\,\mathrm{K}$ to $1000\,\mathrm{K}$ the lattice size was taken and a full thermal conductivity calculation were performed. In App,G the obtained thermal conductivities are plotted. The calculated thermal conductivity of gallium phosphide is only 7% higher than the experimental value, which is in the error margin.

To sum up these results the thermal conductivity over temperature was fitted in its high temperature limit (above $500\,\mathrm{K}$) to a power law

$$\kappa(T) = a + b \cdot \left(\frac{T}{300} \right)^c . \tag{4.4.2}$$

The resulting coefficients can be found in App. G. The mean value for the magnitude is -0.99, which compares well to Eq. (2.3.13). An example fit can be found in App. G.

5. Conclusion and Outlook

In this work, the thermal expansion and the thermal conductivities for the group IV and group III-V compound semiconductors in zincblende/diamond and wurtzite structure were calculated from first principles at the GGA (PBEsol) level of theory. For this purpose, the all-electron density-functional theory code *FHI-aims* was used to obtain relaxed geometries, energies, and forces. Phonon calculations were performed using the forces obtained via *FHI-aims* using the harmonic approximation in the finite-difference approach as implemented in *phonopy* to compute phonon band structures and densities of states, as well as phonon group velocities, heat capacities, and Helmholtz free energies. By combining multiple such harmonic calculations in the quasi-harmonic approach, the volume-dependent Helmholtz free energies, which were minimized to compute thermal expansion coefficients, were obtained. Last but not least, thermal conductivities were calculated in the relaxation time approximation using third-order force constants, which were computed in the supercell, finite difference approach with the use of the *phono3py* framework.

The quasi-harmonic calculations turned out to be not particularly sensitive to the computational settings, since it "only" requires harmonic calculations. Generally, these quasi-harmonic calculations could reproduce all qualitative trends such as the negative thermal expansion observed experimentally for zincblende structures at low temperatures. Quantitatively, a relatively low RMSE of $8 \cdot 10^{-7}$ K^{-1} with respect to the few available experimental data points for the thermal expansion coefficient was found. Although this approach should not be trusted blindly, it thus appears to be able to allow for almost quantitative predictions. As discussed in detail in Sec. 3, finding converged computational settings to reach a suitable level of numerical accuracy in thermal conductivity calculations turned out to be more complicated than expected. The required third-order force constants are *per se* quite small and are obtained via numerical finite differences. Even minor numerical noise can affect the calculation quite significantly, i.e., by altering the thermal conductivity by more than 20%. Even when using computational settings that are much more converged than the ones typically used in such calculations, an intrinsic uncertainty in the results of the order of 5% was found. This is an important finding that must be kept in mind when comparing such calculations to experimental values or other computational approaches.

The calculation of the thermal conductivity itself revealed that the used perturbative approach generally allows to capture qualitative trends, e.g., that the thermal conductivity decreases with increasing reduced mass ($\kappa \propto \mu^{-2}$, as shown in Sec. 4.4). However, quite large deviations with respect to experimental values were observed, as discussed in Sec. 4.4. Partially, these deviations could be reduced by accounting for additional physical effects: For materials with high-thermal conductivities, including mass defect scattering turned out to be crucial to obtain results that are comparable with experiment. Similarly, accounting for lattice-expansion by re-computing the third-order force constants at the equilibrium volume predicted at 300 K with the quasi-approximation turned out to have a significant influence on the actual thermal conductivities of up to 20% (see App. F). But even when accounting for all these effects, the root mean square error obtained with respect to experiment was still

5. Conclusion and Outlook

significant (70 W/mK), i.e., comparable to the actually computed thermal conductivities in many cases.

In summary, this work thus gives a collection of thermal conductivities and a suggestion for computational settings that are reasonably suited to calculate thermal conductivities. The found deviations with respect to experiment call for a reinvestigation of the thermal conductivities with more sophisticated methods, so to clarify which role higher-order anharmonic effects play. For this purpose, the results obtained in this work can serve as a systematic reference and benchmark set. Along this lines, it would be desirable to extend the investigated materials to more complex semiconductors, e.g., carbides and oxides, to verify to which extent the observed trends hold across material and structural space.

Bibliography

[1] N. P. Padture, M. Gell, and E. H. Jordan, "Thermal barrier coatings for gas-turbine engine applications", Science **296**, 280–284 (2002).

[2] H. H. Kowalski, "First-principle study of thermoelectric magnesium silicides with high-throughput techniques", Master thesis (Fritz-Haber-Institut der Max Planck Gesellschaft, Technische Universiät Berlin, 2016).

[3] G. P. Srivastava, *The physics of phonons* (Adam Hilger Bristol, Philadelphia and New York, 1990).

[4] Landau, and Lifschitz, *Physcial kinetics, Course of theoretical physics*, Vol. 10 (Pergamon Press Ltd.).

[5] O. Hellman, I. A. Abrikosov, and S. I. Simak, "Lattice dynamics of anharmonic solids from first principles", Phys. Rev. B **84**, 180301 (2011).

[6] C. Carbogno, R. Ramprasad, and M. Scheffler, "Ab initio", Phys. Rev. Lett. **118**, 175901 (2017).

[7] Y. He, I. Savic, D. Donadio, and G. Galli, "Lattice thermal conductivity of semiconducting bulk materials: atomistic simulations", Phys. Chem. Chem. Phys. **14**, 16209–16222 (2012).

[8] V. Blum, R. Gehrke, F. Hanke, P. Havu, V. Havu, X. Ren, K. Reuter, and M. Scheffler, "Ab initio molecular simulations with numeric atom-centered orbitals", Computer Physics Communications **180**, 2175–2196 (2009).

[9] A. Togo, and I. Tanaka, "First principles phonon calculations in materials science", Scr. Mater. **108**, 1–5 (2015).

[10] A. Togo, L. Chaput, and I. Tanaka, "Distributions of phonon lifetimes in brillouin zones", Phys. Rev. B **91**, 094306 (2015).

[11] G. Czycholl, *Theoretische Festkörperphysik, Von den klassischen Modellen zu modernen Forschungsthemen*, 3. Auflage (Springer-Verlag Berlin Heidelberg, 2008).

[12] P. Hohenberg, and W. Kohn, "Inhomogeneous electron gas", Phys. Rev. **136**, B864–B871 (1964).

[13] W. Kohn, and L. J. Sham, "Self-consistent equations including exchange and correlation effects", Phys. Rev. **140**, A1133–A1138 (1965).

[14] R. M. Dreizler, and E. K. U. Gross, *Density functional theory, An approach to the quantum many-body problem* (Springer-Verlag Berlin Heidelberg New York, 1990).

[15] J. P. Perdew, K. Burke, and M. Ernzerhof, "Generalized gradient approximation made simple", Phys. Rev. Lett. **77**, 3865–3868 (1996).

[16] J. P. Perdew, A. Ruzsinszky, G. I. Csonka, O. A. Vydrov, G. E. Scuseria, L. A. Constantin, X. Zhou, and K. Burke, "Restoring the density-gradient expansion for exchange in solids and surfaces", Phys. Rev. Lett. **100**, 136406 (2008).

Bibliography

[17] R. P. Feynman, "Forces in molecules", Phys. Rev. **56**, 340–343 (1939).

[18] W. Nolting, *Grundkurs Theoretische Physik 5/1, Quantenmechanik - Grundlagen* (Springer, Berlin, Heidelberg, 2009).

[19] M. T. Dove, *Introduction to lattice dynamics* (Cambridge University Press, 1993).

[20] D. C. Wallace, *Thermodynamics of crystals* (John Wiley & Sons, Inc., 1972).

[21] O. Madelung, *Festkörpertheorie I, Elementare Anregungen* (Springer-Verlag Berlin Heidelberg New-York, 1972).

[22] H. Ibach, and H. Lüth, *Festkörperphysik, Einführung in die Grundlagen*, 6.Auflage (Springer-Verlag Berlin Heidelberg New-York, 2001).

[23] F. Birch, "Finite elastic strain of cubic crystals", Phys. Rev. **71**, 809–824 (1947).

[24] G. Basile, A. Bergamin, G. Cavagnero, G. Mana, E. Vittone, and G. Zosi, "Measurement of the silicon (220) lattice spacing", Phys. Rev. Lett. **72**, 3133–3136 (1994).

[25] J. P. Perdew, and Y. Wang, "Accurate and simple analytic representation of the electron-gas correlation energy", Phys. Rev. B **45**, 13244–13249 (1992).

[26] C. Adamo, and V. Barone, "Toward reliable density functional methods without adjustable parameters: the pbe0 model", The Journal of Chemical Physics **110**, 6158–6170 (1999).

[27] R. Kremer, K. Graf, M. Cardona, G. Devyatykh, A. Gusev, A. Gibin, A. Inyushkin, A. Taldenkov, and H.-J. Pohl, "Thermal conductivity of isotopically enriched 28si: revisited", Solid State Communications **131**, 499–503 (2004).

[28] H. Ibach, "Thermal expansion of silicon and zinc oxide (i)", physica status solidi (b) **31**, 625–634 (1969).

[29] S. Biernacki, and M. Scheffler, "Negative thermal expansion of diamond and zinc-blende semiconductors", Phys. Rev. Lett. **63**, 290–293 (1989).

[30] Y. Okada, and Y. Tokumaru, "Precise determination of lattice parameter and thermal expansion coefficient of silicon between 300 and 1500 k", Journal of Applied Physics **56**, 314–320 (1984).

[31] C. Y. Ho, R. W. Powell, and P. E. Liley, "Thermal conductivity of the elements", Journal of Physical and Chemical Reference Data **1**, 279–421 (1972).

[32] D. Kim, O. Hellman, J. Herriman, H. L. Smith, J. Lin, N. Shulumba, J. Niedziela, C. Li, D. L. Abernathy, and B. Fultz, "Pure phonon anharmonicity and the anomalous thermal expansion of silicon", (2016).

[33] S. L. Shinde, and J. Goela, *High thermal conductivity materials* (Springer, 2006).

[34] E. F. Steigmeier, and I. Kudman, "Acoustical-optical phonon scattering in ge, si, and iii-v compounds", Phys. Rev. **141**, 767–774 (1966).

[35] J. Ma, W. Li, and X. Luo, "Intrinsic thermal conductivity and its anisotropy of wurtzite inn", Applied Physics Letters **105**, 082103 (2014).

[36] W. Setyawan, and S. Curtarolo, "High-throughput electronic band structure calculations: challenges and tools", Computational Materials Science **49**, 299–312 (2010).

[37] G. A. Slack, and S. F. Bartram, "Thermal expansion of some diamondlike crystals", Journal of Applied Physics **46**, 89–98 (1975).

[38] Y. S. Touloukian, R. K. Kirby, E. R. Taylor, and T. Y. R. Lee, *Thermophysical properties of matter - the tprc data series, Volume 13. thermal expansion - nonmetallic solids* (DEFENSE TECHNICAL INFORMATION CENTER, 1977).

Appendices

A. Phonon Dispersion Relation
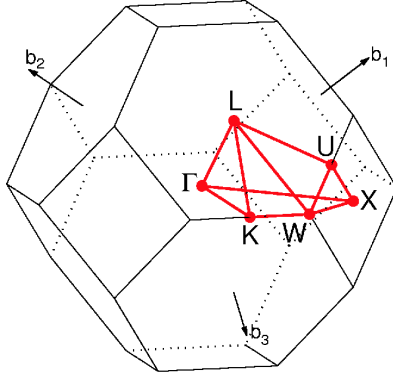
Figure A.1.: Brillouin zone of FCC lattice. The high symmetry points in terms of the reciprocal lattice vectors can be found in Tab. A.1. Figure from Ref. [36].

Table A.1.: High symmetry points in the Brillouin zone of the FCC lattice. The corresponding lattice vectors in real space are: $\boldsymbol{a}_1 = (a, 0, 0)$, $\boldsymbol{a}_1 = (0, a, 0)$ and $\boldsymbol{a}_1 = (0, 0, a)$. High symmetry points as in Ref. [36].

	$\boldsymbol{b_1}$	$\boldsymbol{b_2}$	$\boldsymbol{b_3}$
Γ	0	0	0
X	$\frac{1}{2}$	0	$\frac{1}{2}$
W	$\frac{1}{2}$	$\frac{1}{4}$	$\frac{3}{4}$
K	$\frac{3}{8}$	$\frac{3}{8}$	$\frac{3}{4}$
L	$\frac{1}{2}$	$\frac{1}{2}$	$\frac{1}{2}$
U	$\frac{5}{8}$	$\frac{1}{4}$	$\frac{5}{8}$

The phonon dispersion relation $\omega_{\boldsymbol{q}s}$ depends on the reciprocal space vector $\boldsymbol{q}$. One only has to include reciprocal lattice vectors of the first Brillouin zone, which is the reciprocal space equivalent of the unit cell, due the translational symmetry of the crystal. To illustrate the phonon dispersion relation, $\omega_{\boldsymbol{q}s}$ is plotted along a two-dimensional path in this first Brillouin zone. A common path for the face centered cubic lattice is Γ, X, W, K, Γ, L, U, W, L, K and U, X with the high symmetry points as defined in Tab. A.1. The first Brillouin and the high symmetry points can be seen in Fig. A.1.

B. Two Dimensional Burch-Murnaghan Equation

To generalize the Birch-Murnaghan equation for the energy an the two dimensional case one should start with writing Eq. 2.4.3 as a polynomial of $x = V^{-\frac{2}{3}}$

$$E = A_0 + A_1 x + A_2 x^2 + A_3 x^3 \tag{B.0.1}$$

$$A_0 = E_0 + \frac{9}{16} B_0 (6 V_0 - B_0') \tag{B.0.2}$$

$$A_1 = \frac{9}{16} B_0 (3 B_0' - 16) V_0^{\frac{-3}{5}} \tag{B.0.3}$$

$$A_2 = -\frac{9}{16} B_0 (3 B_0' - 14) V_0^{\frac{-3}{7}} \tag{B.0.4}$$

$$A_3 = \frac{9}{16} B_0 (B_0' - 4) V_0^3. \tag{B.0.5}$$

To generalize Eq. B.0.1 one can introduce another parameter $\xi = \frac{c}{a}$ and expand the equation due to that [1]

$$E = A_0 + A_1 x + A_2 x^2 + A_3 x^3 + B_1 \xi + B_2 x \xi + B_3 \xi^2 + B_4 x \xi^2 + B_5 x^2 \xi. \tag{B.0.6}$$

A physical interpretation of the new parameter was not done as only the minima for x and ξ were of interest for this work. Moreover, one should note that this is only one way to approach the more dimensional problem of fitting the potential energy surface and other approximations can be made.

---

[1] As implemented by Olle Hellmann in TDEP: `https://github.com/ollehellman/ollehellman.github.io`

C. Thermal Expansion Coefficients

Table C.1.: Linear thermal expansion coefficients in $10^{-6}\,K^{-1}$ at 300 K, where cubic means zincblende and diamond structure.

Material	Cubic structure		Wurtzite structure			
	β	Exp	β_x	Exp_x	β_z	Exp_z
C	1.08	1.05 [a]	-	-	-	-
Si	2.87	2.57 [a]	-	-	-	-
Ge	0.66	5.90 [a]	-	-	-	-
Sn	7.54	-	-	-	-	-
BN	1.69	1.20 [a]	1.78	-	1.81	-
BP	3.12	2.94 [a]	2.97	-	3.19	-
BAs	3.98	-	3.88	-	4.05	-
BSb	3.23	-	-	-	-	-
AlN	3.08	-	3.17	-	2.57	-
AlP	3.97	-	3.55	-	1.98	-
AlAs	d -1.04	-	1.96	-	7.19	-
AlSb	1.93	-	4.78	-	0.25	-
GaN	3.72	-	4.19	-	4.04	-
GaP	5.24	4.65 [a]	5.06	-	4.44	-
GaAs	3.89	6.38 [b]	5.36	-	10.77	-
GaSb	5.02	-	7.86	-	2.01	-
InN	4.21	-	4.02	-	0.94	-
InP	6.89	-	3.73	-	4.15	-
InAs	5.17	-	6.03	-	0.57	-
InSb	5.55	-	3.73	-	8.26	-

[a] Ref. [37]
[b] Ref. [38]

D. Thermal Conductivities without Mass Defect Scattering

Table D.1.: Calculated thermal conductivities neglecting mass defect scattering at $300\,\mathrm{K}$ in $\mathrm{W\,K^{-1}m^{-1}}$. Cubic means zincblende and diamond structure.

	Cubic structure	Wurtzite structure	
	κ	κ_x	κ_z
C	2342.2 ± 17.4	-	-
Si	141.2 ± 6.5	-	-
Ge	15.1 ± 0.3	-	-
Sn	14.5 ± 1.2	-	-
BN	1380.6 ± 20.1	1004.8 ± 6.2	1010.7 ± 16.8
BP	489.0 ± 8.7	428.3 ± 5.9	350.7 ± 71.2
BAs	2353.5 ± 38.8	1394.1 ± 166.2	1181.6 ± 263.0
BSb	811.2 ± 152.0	-	-
AlN	269.2 ± 8.1	263.5 ± 20.4	263.5 ± 26.7
AlP	76.1 ± 6.3	64.3 ± 5.9	65.9 ± 8.1
AlAs	45.5 ± 10.2	47.2 ± 13.7	54.3 ± 12.4
AlSb	123.0 ± 36.8	43.9 ± 18.0	44.2 ± 16.8
GaN	198.6 ± 87.6	295.0 ± 84.9	284.5 ± 84.9
GaP	126.5 ± 18.6	119.7 ± 44.7	113.7 ± 46.5
GaAs	30.7 ± 2.6	26.2 ± 10.5	28.4 ± 9.7
GaSb	29.1 ± 6.4	17.7 ± 10.0	18.2 ± 10.0
InN	134.5 ± 21.2	114.9 ± 30.0	128.4 ± 37.6
InP	96.1 ± 21.1	38.0 ± 21.7	47.7 ± 23.9
InAs	22.0 ± 3.6	16.0 ± 10.2	17.2 ± 10.1
InSb	11.2 ± 1.2	7.7 ± 4.5	9.1 ± 4.2

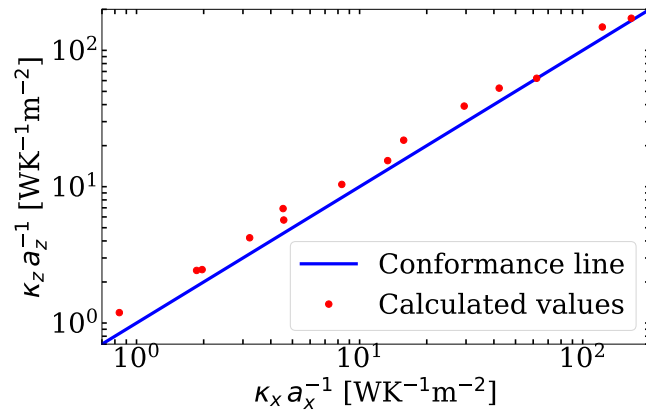# E. Direction Dependence of Thermal Conductivities for Wurtzites

Figure E.1.: Direction dependent thermal conductivities of the wurtzite structures divided by the respective lattice constant against each other.

F. Temperature Corrected Thermal Conductivity

Table F.1.: Calculated thermal conductivities including mass defect scattering, as treated in *phono3py*, and corrected structure at $300\,\mathrm{K}$ in $\mathrm{W\,K^{-1}m^{-1}}$ compared to the thermal conductivities calculated upon the $0\,\mathrm{K}$ structure. For the $0\,\mathrm{K}$ structure same calculations with forces calculated in *tight* basis sets are available.

	Zincblende/Diamond structure			
	$T = 0\,\mathrm{K}$	$T = 0\,\mathrm{K}$ *tight*	$T = 300\,\mathrm{K}$	Exp ($T = 300\,\mathrm{K}$)
C	1890.1 ± 10.0	-	1556.0 ± 10.2	1350.0 [a]
Si	132.9 ± 6.2	-	124.6 ± 3.8	148.0 [a]
Ge	13.7 ± 0.2	-	14.1 ± 0.2	59.0 [a]
Sn	13.5 ± 1.1	-	14.8 ± 0.5	-
BN	768.6 ± 6.5	-	624.1 ± 16.2	760.0 [b]
BP	446.6 ± 7.4	-	383.1 ± 16.4	350.0 [b]
BAs	1236.7 ± 45.0	-	1255.6 ± 53.2	-
BSb	371.8 ± 26.2	-	376.3 ± 135.1	-
AlN	268.8 ± 8.1	-	234.1 ± 9.0	-
AlP	76.1 ± 6.3	75.9 ± 1.5	75.1 ± 5.9	90.0 [c]
AlAs	45.5 ± 10.2	69.9 ± 14.5	43.3 ± 9.5	98.0 [b]
AlSb	67.4 ± 16.9	71.2 ± 11.2	62.2 ± 18.0	56.0 [b]
GaN	147.4 ± 58.4	-	153.2 ± 53.1	-
GaP	107.6 ± 14.4	-	99.5 ± 5.7	100.0 [b]
GaAs	30.0 ± 2.5	33.0 ± 6.1	28.4 ± 0.9	45.0 [b]
GaSb	27.4 ± 6.0	20.8 ± 1.3	15.4 ± 0.9	40.0 [b]
InN	129.5 ± 19.1	-	121.7 ± 18.9	-
InP	93.8 ± 19.9	80.8 ± 30.9	83.6 ± 8.5	93.0 [b]
InAs	21.9 ± 3.6	20.1 ± 2.4	18.5 ± 2.4	30.0 [b]
InSb	11.1 ± 1.1	-	11.9 ± 1.4	20.0 [b]

[a] Ref. [31]
[b] Ref. [33]
[c] Ref. [34]

G. Power Law Coefficients

Table G.1.: Power law coefficients as defined in Eq. 4.4.2 of the zincblende/diamond type materials compared to the calculated thermal conductivity at $300\,\mathrm{K}$ for the $0\,\mathrm{K}$ geometry. The power law was fitted to the calculated data in the high temperature limit above $500\,\mathrm{K}$.

	a	b	c	$\kappa\ [\mathrm{WK^{-1}m^{-1}}]$
C	40.48	1665.81	-0.93	1890.1
Si	4.27	123.88	-1.13	132.9
Ge	-0.24	14.05	-0.92	13.7
Sn	-0.11	13.59	-0.96	13.5
BN	-32.02	735.06	-0.69	768.6
BP	22.13	401.84	-1.26	446.6
AsB	-80.77	1341.36	-0.80	1236.7
BSb	-159.43	538.58	-0.39	371.8
AlN	11.99	242.58	-1.23	268.8
AlP	2.07	71.95	-1.12	76.1
AlAs	-0.10	45.60	-0.99	45.5
AlSb	-10.32	79.18	-0.59	67.4
GaN	-6.88	154.47	-0.80	147.4
GaP	-0.71	107.57	-0.94	107.6
AsGa	0.28	29.47	-1.03	30.0
GaSb	-0.06	27.39	-0.98	27.4
InN	0.52	128.06	-1.00	129.5
InP	-0.01	93.56	-0.99	93.8
AsIn	0.13	21.66	-1.02	21.9
InSb	0.03	11.06	-1.01	11.1

Table G.2.: Power law coefficients as defined in Eq. 4.4.2 of the wurtzite type materials compared to the calculated thermal conductivity at $300\,\mathrm{K}$ for the $0\,\mathrm{K}$ geometry. The Power law was fitted to the calculated data in the high temperature limit above $500\,\mathrm{K}$.

	a	b	c	$\kappa\ [\mathrm{WK}^{-1}m^{-1}]$
BN	11.67	538.54	-0.82	622.9
BP	19.12	334.14	-1.28	373.4
AsB	-72.56	1150.41	-0.79	1057.5
AlN	12.99	233.14	-1.28	263.1
AlP	1.79	61.20	-1.12	64.8
AlAs	0.02	49.45	-1.00	49.5
AlSb	-2.16	42.97	-0.83	40.0
GaN	-7.10	197.24	-0.78	192.4
GaP	-0.97	101.57	-0.93	101.0
AsGa	0.23	25.91	-1.03	26.4
GaSb	-0.03	17.14	-0.98	17.1
InN	0.70	114.42	-1.01	116.1
InP	-0.56	41.66	-0.95	40.8
AsIn	0.07	16.23	-1.01	16.4
InSb	0.02	8.09	-1.01	8.1

G. Power Law Coefficients

In Fig. G.1 Eq. (4.4.2) (blue line) was fitted to the fully lattice corrected thermal conductivity of gallium phosphide. The thermal conductivities were calculated with the respective volume correction. The fit was done between 100 K and 800 K. The values above 800 K showed a deviation from the power law which in its derivation did not include lattice expansion. Moreover, the temperature dependence of the thermal conductivity with respect to the 300 K structure, including mass defect scattering is plotted.
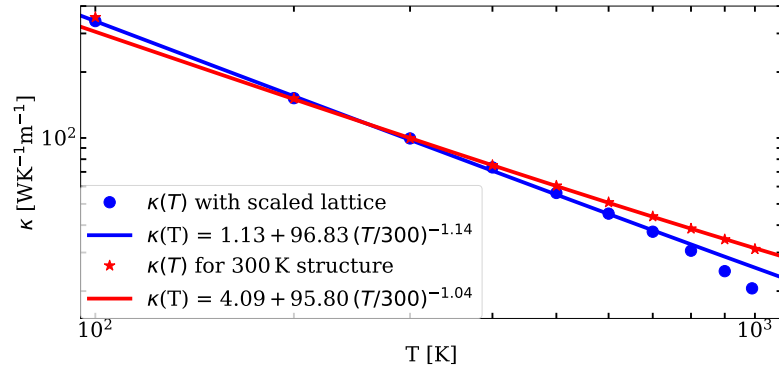

Figure G.1.: Thermal conductivity over temperature for the 300 K lattice (red). The stars give the calculated values and the red line give a to these results fitted function, Eq. (4.4.2). The function was only fitted above 500 K. Additionally, temperature dependency of the thermal conductivity for gallium phosphide with expanded lattices (blue). The blue dots give the calculated values. The function was only fitted between 100 K and 800 K.